JGR Solid Earth

RESEARCH ARTICLE
10.1029/2018JB017143

Special Section:
Slow Slip Phenomena and Plate Boundary Processes

Seismic Velocity Change Patterns Along the San Jacinto Fault Zone Following the 2010 *M*7.2 El Mayor-Cucapah and *M*5.4 Collins Valley Earthquakes

G. Hillers[1], M. Campillo[2], F. Brenguier[2], L. Moreau[2], D. C. Agnew[3], and Y. Ben-Zion[4]

[1]Institute of Seismology, University of Helsinki, Helsinki, Finland, [2]Institut des Sciences de la Terre, Université Grenoble-Alpes, Grenoble, France, [3]Scripps Institution of Oceanography, University of California, San Diego, La Jolla, CA, USA, [4]Department of Earth Sciences, University of Southern California, Los Angeles, CA, USA

Key Points:
- We observe seismic velocity change patterns that vary along and across the San Jacinto fault zone
- The time and frequency dependence of the changes suggests an upward migrating deformation pattern
- Together with strainmeter signals these results indicate a response to two deep creep events

Supporting Information:
- Supporting Information S1
- Data Set S1

Correspondence to:
G. Hillers,
gregor.hillers@helsinki.fi

Citation:
Hillers, G., Campillo, M., Brenguier, F., Moreau, L., Agnew, D. C., & Ben-Zion, Y. (2019). Seismic velocity change patterns along the San Jacinto fault zone following the 2010 *M*7.2 El Mayor-Cucapah and *M*5.4 Collins Valley earthquakes. *Journal of Geophysical Research: Solid Earth*, *124*, 7171–7192. https://doi.org/10.1029/2018JB017143

Received 6 DEC 2018
Accepted 7 JUN 2019
Accepted article online 13 JUN 2019
Published online 31 JUL 2019

Abstract We study temporal changes of seismic velocity (dv/v) in the crust around the central section of the San Jacinto fault zone (SJFZ), Southern California. Focusing on a 200-day-long period around April 2010, our analysis resolves two tens-of-days-long successive episodes of reduced velocities that are compatible with signals from the long base strainmeter at the Piñon Flat Observatory. The imaged dv/v sequences are proxies for evolving material properties in the crust surrounding the SJFZ. The temporal and the spatial coincidence of the observed dv/v patterns with the occurrence of two proposed creep episodes suggest that the relative velocity changes reflect the response to deep creep events that follow the *M*7.2 El Mayor-Cucapah earthquake and the *M*5.4 Collins Valley earthquake that occurred 94 days later on the San Jacinto fault. The main slip during the creep events was proposed to occur below 10-km depth. Wavefield properties suggest sensitivity to medium changes above this source zone, in the top 10 km. The distribution of the obtained dv/v reductions shows a strong difference between large values to the west of the SJFZ and significantly smaller amplitudes to the east. The similarity to the seasonal velocity change pattern implies that the results are likely controlled by the contrast of mechanical properties across the fault, such as fault-perpendicular shear modulus variations. Our analysis extends the spectrum of methods that can be used to study earthquake interaction, fault zone rheology and dynamics, triggering, and the interplay between creep episodes and earthquakes.

Plain Language Summary Motion along geologic fault zones not only occurs during small and large potentially devastating earthquakes. Some faults creep aseismically, which means the slip motion is too slow to generate earthquake waves. To develop a more complete understanding of fault behavior, it is important to detect and locate such creep transients. A particularly interesting problem is how earthquakes and episodic creep events, which tend to occur in a zone below the earthquakes, interact with each other. Creep events are usually detected using satellite-based methods. In this study we applied the most modern ambient seismic wavefield analysis techniques to first detect and locate changes in the rock properties around a continental strike slip fault, the San Jacinto fault, Southern California, that are caused by two successive deep creep events along that fault. These results are supported by data from a colocated deformation meter that picked up signals from the same creep events that are thought to be triggered, initiated by the two earthquakes indicated in the title. The observed deformation patterns—they are not uniform along and across the fault—and their temporal evolution can help us better understand the processes that happen on and off faults in earthquake-prone regions.

1. Introduction

The 4 April 2010 *M*7.2 El Mayor-Cucapah (EMC) earthquake occurred on the Laguna Salada fault system in Baja California, Mexico (Hauksson et al., 2011; Wei, Fielding, et al., 2011; Figure 1a, blue star). It triggered widespread phenomena on many faults in the well-instrumented Southern California plate boundary region. Analyses of evolving aftershocks and postseismic deformation in the Yuha Desert to the northwest of the EMC rupture indicate that deep localized afterslip propagated in this direction and was followed by a volumetric diffusion-like process (Ross et al., 2017). The triggered aftershocks in the Yuha Desert include the *M*5.7 Ocotillo event 72 days later on 15 June 2010 (Figure 1a, purple star). Observed UAVSAR satellite and GPS data in the Yuha Desert show asymmetric migrating deformation patterns after the EMC event

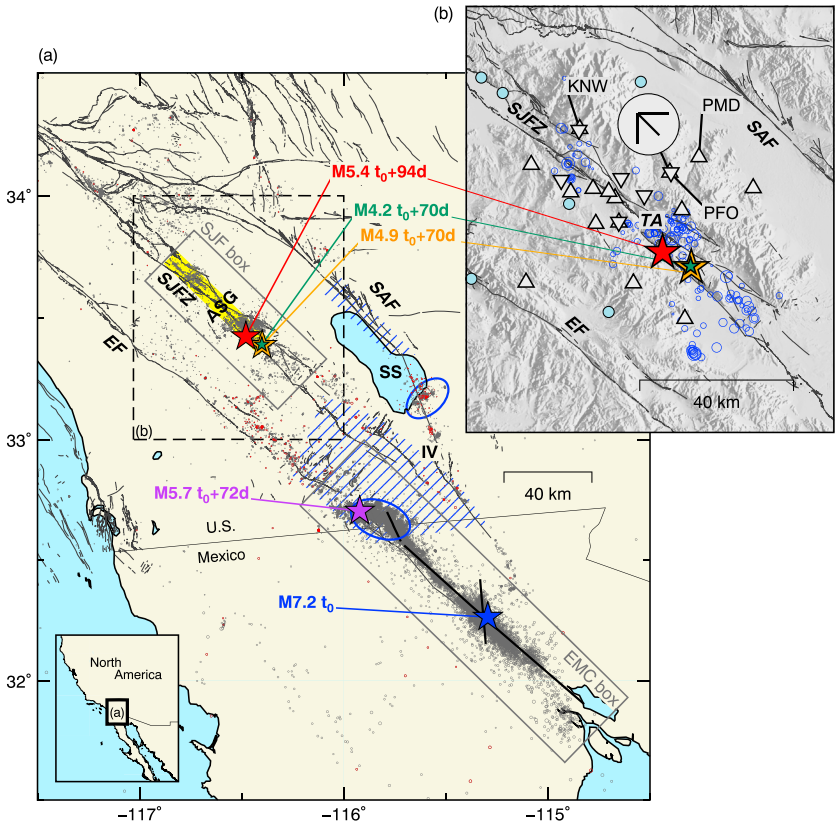

Figure 1. (a) Map of the study area. Gray circles indicate 2010 seismicity. Red circles indicate seismicity outside the two grey boxes in the 5 days after the EMC event that led to the spike at t_0, the day of the EMC event, in the red data in Figure 2b. Stars indicate $M > 4$ events. Their occurrence is indicated in the following figures with the correspondingly colored vertical lines. Blue, purple, and red stars indicate the M7.2 EMC, M5.7 Ocotillo, and M5.4 Collins Valley earthquakes, respectively. Black lines are mapped fault traces. The black lines in the EMC box show the trace of the finite source model (Mai & Thingbaijam, 2014; Wei, Fielding, et al., 2011). Blue ellipses and hatched regions denote areas discussed in section 1. The ellipse around the Ocotillo event indicates the Yuha Desert region. The ellipse at "SS" indicates the Salton Sea Geothermal Field. Shallow slip has been triggered on faults in the hatched areas to the left of the "IV" and below the "SAF" labels. Deep slow slip has been inferred along the yellow indicated SJFZ fault segment that extends to the orange star. EMC = El Mayor-Cucapah; EF = Elsinore fault; SJFZ = San Jacinto fault zone; ASG = Anza seismic gap; SAF = San Andreas fault; SS = Salton Sea; IV = Imperial Valley. (b) Enlarged study area. Triangles and inverted triangles indicate surface and borehole stations. Blue circles indicate seismicity in the SJF box in (a) in the 5 days after the EMC event that led to the spike at t_0 in the black data in Figure 2b. PFO, KNW, and PMD are stations referred to in the text. The tripod indicates the configuration of the long base strainmeter at the PFO site. Light blue dots indicate hot springs. TA = trifurcation area.

that are more pronounced to the northeast of the EMC rupture, along with triggered shallow slip by the Ocotillo aftershock that extends to the Elsinore fault (Donnellan et al., 2018). To the north of the rupture the EMC event triggered shallow slip on multiple larger and minor faults in the greater Salton Trough area and in the Imperial Valley (Donnellan et al., 2014; Wei, Sandwell, et al., 2011), similar to previous regional earthquakes (Hudnut et al., 1989; Rymer et al., 2002). The coseismic timing of the slip and the lack of significant afterslip suggest that the triggering involves waves excited by the EMC event. Dislocation modeling confined the triggered slip to the uppermost few kilometers within the velocity strengthening zone that is characterized by unconsolidated sediments with high pore pressure (Wei, Sandwell, et al., 2011). Only at the southern end of the Imperial fault was the initial shallow slip followed by fault slip at depth (Donnellan et al., 2014). Seismicity rates in the Salton Sea Geothermal Field increased after the EMC event (Meng & Peng, 2014), and noise-based monitoring resolved seismic velocity reductions in this area at depths between 0.5 and 1.5 km (Taira et al., 2018). Similar to the behavior seen after many medium and large earthquakes, the relative velocity variations dv/v are characterized by a coseismic drop followed by a gradual recovery.

Here we focus on the effects of the EMC event in the San Jacinto fault zone (SJFZ) region. We apply noise analysis techniques to data from 21 seismic stations to study two tens-of-days-long transient seismic velocity change episodes around the Anza seismic gap (Figure 1a, ASG). The lack of small and moderate to large earthquakes that defines the Anza gap (Sanders & Kanamori, 1984) is attributed to the localized, simple geometry of this relatively straight ~20-km-long locked fault section. This is in marked contrast to the seismically active trifurcation area to the southeast (Figure 1b, TA) where the fault splits into three branches (Cheng et al., 2018; Hauksson et al., 2012; Ross et al., 2017; Trugman & Shearer, 2017). The observed dv/v transients follow the EMC event and the 7 July 2010 M5.4 Collins Valley event that occurred 94 days later at 12-km depth on the SJFZ in the trifurcation area (Figure 1, red star). The study extends the range of dv/v change observations in the region that have been associated with tidal deformation (Hillers, Retailleau, et al., 2015) and seasonal loading (Hillers, Ben-Zion, et al., 2015). The results demonstrate the possibility of probing processes that are associated with faulting and crustal deformation in an area that is characterized by significant seismic hazard.

The obtained relative velocity change patterns differ from previously observed drop-and-recovery responses to earthquakes of shallow material. The dependence of the observed dv/v variations on time, space, frequency, and coda lapse time indicate a complex evolution of the response. We show that the maximum amplitude reductions estimated above ~10 km occur well after the EMC event, decrease from west to east across the Anza gap, and are smallest in the area between the fault and the Piñon Flat Observatory (Figure 1b, PFO). The similarity of this dv/v amplitude distribution to thermally driven seasonal velocity changes (Hillers, Ben-Zion, et al., 2015) suggests that the response is related to the spatially variable lithology and the heterogeneous mechanical properties across the Anza region (Allam & Ben-Zion, 2012; Fang et al., 2016; Lindsey et al., 2014; Sharp, 1967). A comparison of PFO long base laser strainmeter data with the seismic dv/v changes estimated in the same area shows that seismic velocity reductions coincide with volumetric extension periods following the EMC and the Collins Valley events.

Key properties of the observed transient velocity change patterns are compatible with the proposed occurrence of two successive deep (>10 km) aseismic slip events (Inbal et al., 2017). These slip transients have been inferred from seismicity patterns and geodetic signals and are thought to have been triggered by the EMC and the Collins Valley events. Following this scenario the dv/v changes and strain signals likely reflect the response to these deep creep episodes of the crust around the San Jacinto fault, albeit in a depth interval above the main slipping zones. Our results show that the combined analysis of high quality strain data and seismic dv/v observations can provide additional constraints on aseismic deformation in a strike-slip faulting environment and can therefore contribute to our understanding of triggering processes and earthquake and fault interactions on regional and local scales.

In section 2 we outline the analysis methods used. Section 3 contains a discussion of mechanisms that could affect the resolution of the transient velocity change patterns. After we demonstrate that the signals are not controlled by the wavefield changes associated with the EMC aftershock activity, we separate the slow slip responses from seasonal variations and analyze the frequency and lapse time dependence (section 4), estimate the spatial distribution and the depth of the time-dependent velocity changes (section 5), and compare the seismic velocity change time series to PFO strainmeter data (section 6). The results and implications are discussed in the final section 7.

2. Seismic Data and Analysis

We process data from 15 three-component broadband surface stations of the Anza network (BZN, CRY, FRD, KNW, LVA2, PFO, RDM, SND, TRO, and WMC) and California Integrated Seismic Network (BOR, DNR, PLM, PMD, and TOR) and from six Earthscope/UNAVCO Plate Boundary Observatory (PBO) three-component 2-Hz sensors (B081, B082, B084, B086, B087, and B093) that are installed in boreholes between 120 and 230-m depth around the Anza seismic gap in the SJFZ area (Figure 1b). To study potential dependencies between properties of the ambient wavefield and the observed dv/v variations, we consider cataloged information on the seismicity in the Southern California plate boundary region (Hauksson et al., 2012) together with wavefield markers (Figure 2) and properties of the noise cross-correlations analyzed for the dv/v estimates (Figure 3).

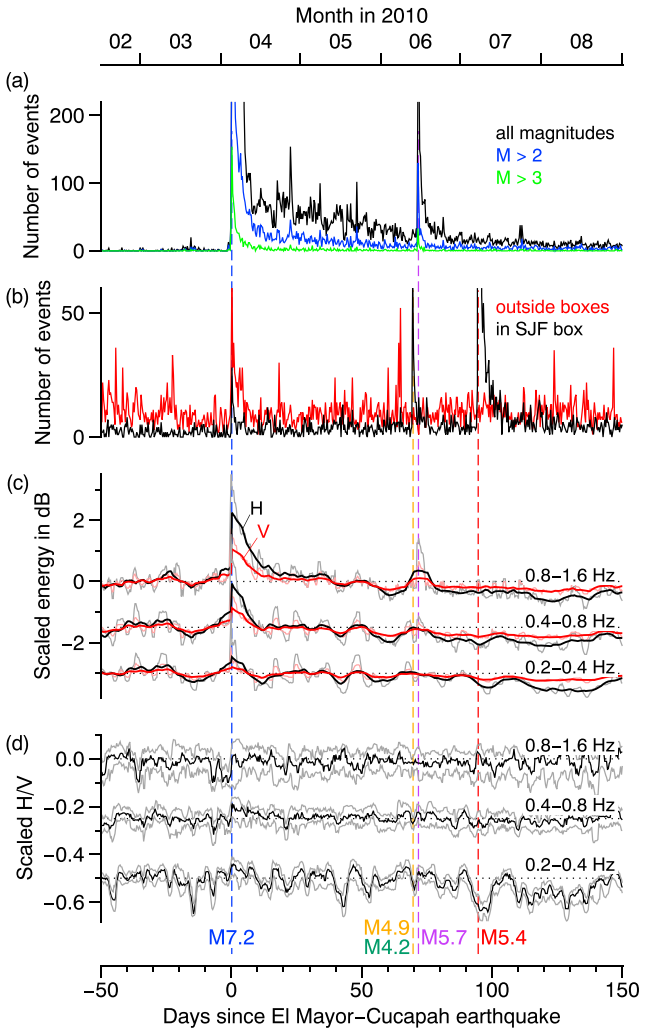

Figure 2. (a) Temporal evolution of the magnitude-dependent seismicity in the EMC box in Figure 1a. The ordinate is clipped. (b) Black data are events in the SJF box in Figure 1a. The corresponding distribution of seismicity in the 5 days after the EMC event is indicated in Figure 1b, blue circles. Red data correspond to the seismicity in Figure 1a that is not in the SJF box and not in the EMC box. The corresponding distribution of seismicity in the 5 days after the EMC event is indicated by the red circles in Figure 1a. The histograms in (a) and (b) show the number of events in 8-hr intervals. (c) H and V energy estimates in three frequency bands. Thin lines are ±1-point median filtered 8-hr data. Thick lines are ±2-day running averages. (d) H/V energy ratios in 8-hr intervals in three frequency bands. Black lines are the network median, and the gray lines are the 0.2 and 0.8 quantiles. In (c) and (d) data are on the same scale but offset for clarity. The dotted lines indicate the median level in the 50 days before t_0. Below average levels at later times reflect a seasonal excitation effect. The vertical lines indicate the occurrence of the correspondingly colored events in Figure 1a. EMC = El Mayor-Cucapah; SJF = San Jacinto fault.

2.1. Wavefield Markers

To compute single-station wavefield markers from surface station data, we first high-pass filter daily seismograms above 0.05 Hz. We split these records from each station and component into 96 15-min windows and estimate the spectral power. The horizontal power H is the sum of the north and east component estimates, and the vertical power V uses the Z-channel data. H and V are estimates of the arriving seismic energy. The ratio H/V is obviously related to the kinetic energy ratio H^2/V^2 which itself is a proxy for the S wave to P wave energy ratio where the spatial derivatives cannot be carried out (Hennino et al., 2001; Shapiro et al., 2000).

From the 32 values per 8 hr we can take any quantile of the three H, V, H/V estimates for each frequency and average over three frequency ranges 0.2–0.4, 0.4–0.8, and 0.8–1.6 Hz and finally over all stations in the network. Figure 2c shows the resulting 0.9 quantile network averages using an additional ±1-point running median filter (thin lines), that is again smoothed with a moving average (thick lines) to better highlight the long-term trend. The time series have been split at the time of the EMC earthquake for the temporal averaging to highlight the effect of the increased aftershock seismicity. H and V values are in decibel before being scaled by the median energy in the 50 days before the EMC event. For the H/V ratios in Figure 2d we show the 0.2, 0.5, and 0.8 network quantiles on a linear amplitude scale. The time series are scaled by the respective median energy in the 50 days before the EMC event. A below-average level for the low frequencies at later times ($t > 80$ days) reflects the seasonal energy variation.

2.2. Cross-Correlation Functions

For the seismic velocity change analysis we make two databases of noise cross-correlation functions between all sensors within 40-km distance of each other using daily seismic records from 2008 to 2015 following the procedure of Hillers, Ben-Zion, et al. (2015), Poli et al. (2012), and Zigone et al. (2015). We first remove the instrument response. Processing is then applied to 1-hr-long windows. We discard 0.05-Hz high-pass filtered hourly seismograms that contain large amplitudes associated with earthquake signals or other transients or data acquisition problems. This transient detection is based on markers of the amplitude distribution in three 20-min-long subwindows. We then apply spectral whitening in the 0.05- to 5-Hz frequency range to the data in each hour-long window (Bensen et al., 2007). For the subsequent time domain amplitude clipping we find that sign-bit clipping yields higher signal-to-noise ratios (SNR) of the resulting correlation functions compared to clipping at some multiple of the standard deviation of the noise amplitude distribution in each processing window. Sign-bit or 1-bit clipping is followed by another 0.05- to 5-Hz bandpass filter before the seismograms are tapered, cross-correlated, and stacked to daily correlation functions.

The first database is made to study seasonal variations between 2008 and 2015 (Figures 4-6). For this we use vertical component data from days 1 to 300 in each year. The daily correlations are stacked over ±2 days and downsampled by a factor of 2. The second database facilitates the high-resolution analysis of the responses to the EMC and Collins Valley events in 2010. This database consists of daily nine-component (9C) correlations between $t_0 - 50$ days and $t_0 + 150$ days, where t_0 is day 94, 4 April 2010 (Figure 7). This window is centered on the 70- to 90-day-long transient following the EMC event, and its extent is limited by the computational cost of the employed dv/v time series estimation described below. The velocity change

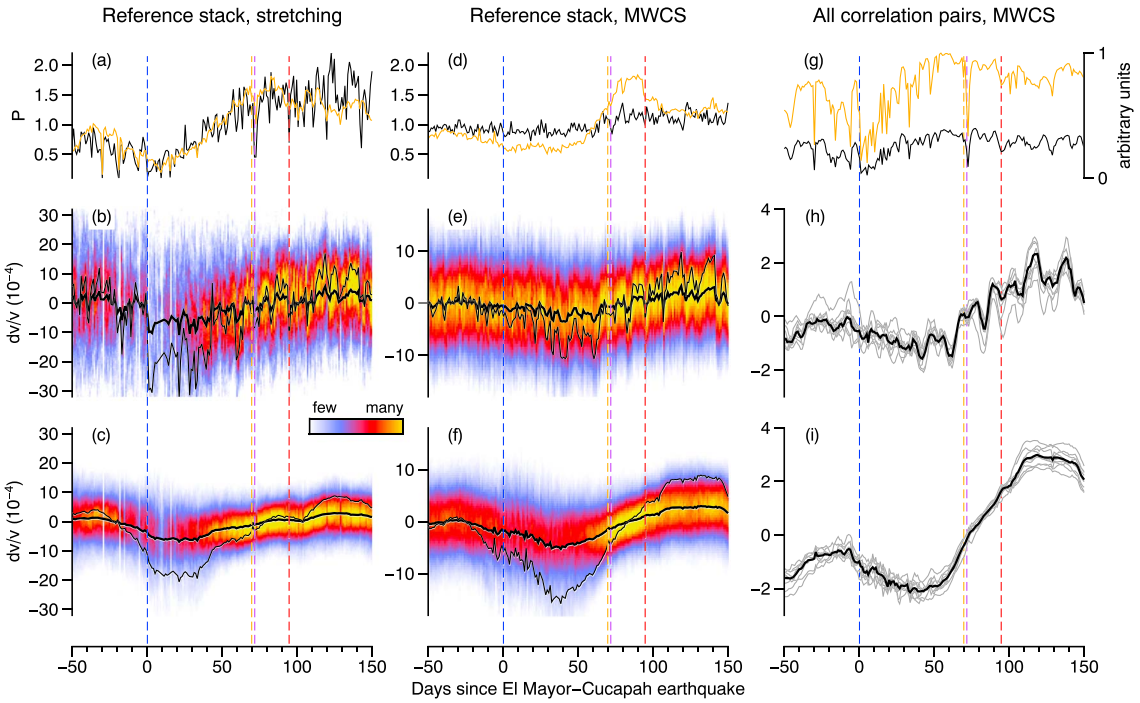

Figure 3. (a) Scaled P values obtained with the time domain stretching method and the average waveform reference approach. Lower P levels before t_0 and the higher levels after 100 days are a seasonal effect. Black and orange lines correspond to the cases in (b) and (c). (b) The colors indicate daily histograms of network and component average dv/v estimates. The thin black line is the factor 3 amplified average indicated by the thick black line to better visualize the variability. (c) The same as in (b) for correlations that have been filtered using the SVDWF. (d)–(f) The same as in (a)–(c) using the frequency domain MWCS technique. (g) Statistics of how often a dv/v estimate based on a correlation function from a given day is used in the inversion. These data show how many dv/v pairs including the correlations functions from a given day have a $cc \geqq 0.85$. Black and orange lines correspond to the cases in (h) and (i). Data are scaled by the peak value of the filtered data. (h) Inversion-based network and component average dv/v estimates using the MWCS technique (black). Gray data indicate network-average results obtained with any one of the nine component pairs. (i) The same as (h) using correlations that have been filtered using the SVDWF. The vertical lines indicate the occurrence of the correspondingly colored events in Figure 1a. All results are from surface station data, nine-component correlations, 0.2–2 Hz, 20–50 s. SVDWF = Singular Value Decomposition based Wiener filter; MWCS = Moving Window Cross Spectral.

signals in this window are imaged in Figure 8, the depth resolution is discussed in Figure 9, and the signals are compared to records from the long base laser strainmeter at the PFO site (Figures 10a–10c).

2.3. Relative Velocity Change Estimates

To assess the robustness of the obtained dv/v results and the sensitivity to wavefield variations, we apply three different approaches for estimating relative velocity change time series from the 2010 9C high-resolution database using surface station data in the 0.2- to 2-Hz frequency range. The associated results are shown columnwise in Figure 3. The first two approaches estimate dv/v changes from variations between a daily correlation function and a reference stack compiled from the correlations in the analysis period. We use the time domain stretching method (Grêt et al., 2005; Lobkis & Weaver, 2003; Sens-Schönfelder & Wegler, 2006) and the frequency domain doublet or Moving Window Cross Spectral (MWCS) technique (Clarke et al., 2011; Poupinet et al., 1984) to measure the travel time changes. In both cases the final estimates shown as black lines in Figures 3b, 3c, 3e, and 3f are the averages over all station and component pairs, whereas the colors in these figures indicate the distributions or histograms of the obtained daily dv/v estimates.

The stretching method is implemented as a grid search over the test waveform distortion or dilation factor ϵ that optimizes the similarity between the 0.2- to 2-Hz bandpass filtered reference stack and the filtered daily correlation in the 20- to 50-s coda lapse time analysis window (Lobkis & Weaver, 2003). This factor ϵ is a direct measure of the targeted dv/v value. For the frequency domain MWCS dv/v estimates we follow Clarke et al. (2011). This technique applies two regressions. First, the time delay $d\tau$ in an analysis window centered at lapse time τ is computed from the frequency-dependent phase change. We compute this first regression over the phase estimates at frequencies in the 0.2- to 2-Hz range using the unfiltered correlation seismograms. The length of the multiple smaller windows in the 20- to 50-s analysis window scales with the longest period. These smaller windows overlap 80%. The $dv/v = -d\tau/\tau$ estimate is then obtained by

applying a second regression to the systematic increase or decrease of $d\tau$ with τ. For the stretching and for the MWCS method a $\tau_1 - \tau_2$ s processing window (e.g., 20–50 s) implies an analysis of waveforms in the $(-\tau_2) - (-\tau_1)$ s and $\tau_1 - \tau_2$ s windows.

In the third approach the dv/v time series is obtained by inverting estimated changes between all possible pairs of daily correlations (Brenguier et al., 2014; Gómez-García et al., 2018). These individual estimates are obtained with the MWCS technique using the above described procedure. This third approach does not rely on a reference function and relaxes also the assumption of stationary wavefield properties. The number of dv/v estimates used in this approach scales quadratically with the number of days per station and component pair, in contrast to the linear scaling using the reference stack. This can better constrain the dv/v model at times with no or low-quality estimates that can result from wavefield variations. The final dv/v time series is obtained with a standard linear least-squares scheme (Brenguier et al., 2014; Tarantola & Valette, 1982). Weights in the inversion scale with the similarity between the full waveforms. This similarity estimate is the scaled cross-correlation coefficient cc. For a network average, data from all stations and components with $cc \geq 0.85$ are inverted simultaneously for a given frequency band and lapse time window. In the inversion we use a correlation length parameter $\beta = 3$ days. The high similarity of results obtained with β values between 1 and 7 days shows that the final dv/v time series are not sensitive to variations within this range. Significant differences occur only if β is varied over a wide range (Brenguier et al., 2014; Gómez-García et al., 2018). The value employed does not degrade the daily resolution and hence does not affect the discussion of the transient onset. Our results are insensitive to the weighting coefficient α parameter that scales the model covariance matrix in the inversion (Gómez-García et al., 2018). This third approach is also used for the low-resolution seasonal analysis.

2.4. Denoising Correlation Functions

The three measurements are repeated after applying a Singular Value Decomposition based Wiener filter (SVDWF; Moreau et al., 2017) to the noise correlations. The filter removes incoherent data across the daily correlations. In contrast to previous denoising approaches (e.g., Stehly et al., 2011) the filter does not depend on a model or reference waveform. The SVDWF works on the singular values of data patches of size $M \times N$. M is the number of days along the calendar time t axis, and N is the number of samples along the correlation lag time τ axis. It thus works on small regions of the full correlation gather which in this context is interpreted to be an "image." We apply a low-pass filter to the correlation functions that is adapted to the dv/v frequency analysis range—for example, a corner frequency of 3 Hz is used for the 0.2- to 2-Hz range—before the composite image is filtered with a fixed $N = 5$. We use $M = 20$ days to mute fluctuations on the 10-day scale seen in Figure 3h and keep the largest $M/2$ singular values. This window size results in a temporal smoothing on the order of 5 days. As shown in Figures 3c, 3f, and 3i, the significantly improved SNR in the noise correlations leads to better dv/v estimates.

2.5. Quality Marker

In addition to the earthquake catalog and wavefield markers, the indicators obtained from the correlation-based dv/v estimates include a marker P of the peakedness of the daily dv/v distributions for the two reference stack-based approaches. We define P as the ratio between the distribution peak value and the distribution width. The width is estimated as the most narrow interval that contains a high fraction (80%) of the total number of values in the distribution. The peak value and the width are inversely proportional to each other, so the ratio accentuates this trend. Large P indicates peaked, narrow distributions and hence an overall well-constrained component and network average, whereas small P characterizes less consistent or more variable estimates. The P values in Figures 3a and 3d capture the evolution of the color-coded dv/v distributions or histograms in Figures 3b and 3c and Figures 3e and 3f, respectively. Small P values are not problematic as such. They are expected if the spatial dv/v pattern varies on scales that are smaller compared to the network size (Hillers, Husen, et al., 2015; Obermann et al., 2013). However, together with other wavefield markers the temporal variation of P can be indicative of periods with poorer dv/v resolution.

For the inversion-based method, we consider how many dv/v estimates associated with a daily correlation have entered the inversion (Figure 3g). This measure is controlled by the $cc = 0.85$ cutoff threshold.

3. Relation Between Wavefield Variations and Velocity Changes

We find that the main variations in the H and V energy time series are dominated by the EMC aftershock sequence and not by properties of the local seismicity along the SJFZ (section 3.1). In contrast, the partition-

ing marker H/V remains remarkable constant throughout the analysis period. We assess to what degree the wavefield amplitude or energy changes affect the dv/v estimates in the study area (section 3.2).

3.1. Seismicity and Wavefield Changes

The aftershock distribution in the EMC rupture area (EMC box in Figure 1a; data in Figure 2a) exhibits the typical seismicity decay pattern described by the Omori law. The shown magnitude dependence illustrates that the larger aftershocks that excite waves with longer periods decay faster compared to the small magnitude events that have thus a longer lasting effect on the local and regional high-frequency wavefield. This frequency-dependent effect is clearly seen in the H and V energy observed in the study area (Figure 2c). The 0.8- to 1.6-Hz high-frequency wavefield shows excess energy for some 40 days after the main shock, whereas the 0.2- to 0.4-Hz low-frequency estimates are affected only for a few days.

The seismicity increase at t_0 in the areas outside the EMC main shock area and outside the study area (red circles in Figure 1a; red data in Figure 2b) is mainly associated with EMC event triggered activity to the north of the main shock zone along the San Andreas, San Jacinto, and Elsinore faults. Events occurring after t_0 along the San Jacinto fault (blue circles in Figure 1b; black data in Figure 2b) are thought to be triggered by deep creep that is in turn triggered by the EMC event (Inbal et al., 2017). The persistently elevated level of small-magnitude seismicity after the EMC event along the SJFZ is more evident from a more complete detection list obtained with template matching techniques (Meng & Peng, 2014). This seismicity does not exhibit the Omori-type behavior that characterizes the EMC aftershock sequence and the H and V time series. Thus, the local seismicity does not govern the variations in these local wavefield markers. Similarly, the M5.4 Collins Valley event in the San Jacinto fault area 94 days after the EMC event does not affect the high quantile wavefield energy on the here considered timescales.

Interestingly, the high-frequency energy peak 72 days after the EMC event (Figure 2c) is associated with the aftershock sequence of the M5.7 Ocotillo event (Figure 1a, purple star) in the EMC main shock area and not with the two M4.9 and the M4.2 events that occurred 70 days later on 13 June 2010 within 23 s 8–9 km below the network in the study area (Figure 1, orange and green stars). This further highlights the effect of seismicity around the EMC earthquake on the high-frequency wavefield properties in the study area.

In contrast to the H and V amplitude estimates, the H/V wavefield marker exhibits a remarkable stability (Figure 2d) on the 8-hr timescale. The H/V ratio fluctuations are on the order of 10% and therefore similar to the variability that Hennino et al. (2001) report for diffusive earthquake coda averaged over 15 s. The H/V time series are unaffected by the strongly variable seismic energy release. We can discern, perhaps, a very small effect in the first 10–20 days after t_0 in the 0.4- to 0.8-Hz range, where the ratio remains slightly increased and the fluctuations are even smaller. This behavior is compatible with an excess excitation of shear waves due to scattering.

Equipartition—the wavefield state at which all possible modes are randomly excited with equal weight on average (Campillo, 2006)—can only be an asymptotic regime in an open system like the Earth's crust. Equipartition implies equilibration of the used energy ratio marker (Weaver, 1982), but the converse statement does not hold (Paul et al., 2005), because a stable ratio can also result from a constant acting excitation mechanism. We thus cannot conclude that the observed time-independent H/V time series are a signature of equipartition. As shown, however, excitation is not constant, so the stabilized energy ratio is a good indicator "that the field is entering a regime in which total energy is described by a diffusion" (Campillo, 2006). The stability of the H/V ratio in the 10- to 20-day time interval that contains excess earthquake coda wavetrains and the consistency with the stable ratio at the other times together imply that the background noise wavefield has a strong diffusive component (Hennino et al., 2001), which supports the dv/v analysis.

We can expect that the scattered or diffusive propagation regime coexists with a ballistic component (Hillers et al., 2012; Larose et al., 2007). This is likely more pronounced at the longer wavelengths due to longer scattering mean free paths and the proximity of the study area to the pelagic and coastal excitation region (Gerstoft & Tanimoto, 2007; Hillers et al., 2013), in contrast to the better wavefield mixing and the more distributed natural and anthropogenic noise sources at higher frequencies (Hillers & Ben-Zion, 2011; Inbal et al., 2018). A stable anisotropic noise field still supports dv/v monitoring (Hadziioannou et al., 2009). High-precision monitoring is possible even if the azimuthal distribution of the noise propagation direction varies (Colombi et al., 2014), which we can expect in the time intervals of the EMC and Ocotillo aftershock sequences and as a consequence of shifting environmental noise source and anthropogenic activity patterns.

Hence, despite the significant wavefield amplitude changes, and despite the changes in the flux direction associated with the intermittent source region around the EMC rupture, the partitioning of the multiply scattered wavefield in the study area remains relatively constant. This stability supports our application of noise-based analysis techniques.

3.2. Method Comparison

The comparison of wavefield markers and dv/v estimates associated with the three different approaches suggests that the results obtained with the stretching method are biased by the effect of the remote EMC aftershock activity on the wavefield amplitudes in the study area (Zhan et al., 2013). On the other hand, the amplitude variations and the changes in the flux direction do not seem to affect the phase-based dv/v estimates, which is compatible with theoretical and observational work (Colombi et al., 2014) and with the overall stable H/V ratios. These conclusions are drawn from Figure 3 and are further supported by the lapse time-dependent results discussed in Figure 7 that show that the velocity change estimates are related to medium changes, and not to source changes. The conclusions are also compatible with the findings of Hillers, Ben-Zion, et al. (2015) and Hillers, Husen, et al. (2015) who both favored MWCS-based results over stretching method-based results, because changes in the excitation pattern left a much weaker footprint in the MWCS-derived dv/v signals.

We focus on the resolution of the transient signal after the EMC event. This signal is superimposed on the seasonal variation. We see that the abrupt velocity drop obtained with the stretching method coincides with the EMC earthquake (Figure 3b), and then gradually approaches the long-term trend. Similarly, the P value in Figure 3a shows that the consistency over the network drops at t_0 and then recovers over 70 days to the final level. As said, the widening of the distribution is not problematic as such, as it could be associated with lateral variations in the velocity changes. However, the low P values also reflect the removal of many spurious measurements from the distributions that cluster at both ends of the wide ϵ grid search range. That is, the algorithm does not indicate a physically meaningful optimal dilation factor ϵ. This behavior is similar to the evolution of the energy estimates in Figure 2c and suggests that the stretching method provides the least stable estimates because of the wavefield amplitude changes.

In contrast to the coseismic drop, the MWCS dv/v results in Figures 3d–3i show a more gradual velocity decrease on the 30- to 40-day scale after t_0 that is followed by the recovery to the long-term trend. The associated black P values in Figure 3d are remarkably stable and hence insensitive to the observed wavefield changes. The cc-based control parameter in Figure 3g associated with the inversion method shows a significant drop-and-recovery-behavior in the period following t_0 that strongly reflects the EMC aftershock-induced wavefield changes. Importantly, however, in contrast to the stretching method results the associated dv/v estimates in Figure 3h show a different, that is, unaffected, gradual response pattern that is similar to the results of the MWCS reference stack approach in Figure 3e.

We repeat this analysis using correlations that have been filtered with the SVDWF (Figures 3c, 3f, and 3i). All results are cleaner and significantly improved, although the filter cannot completely remove the bias from the stretching results at the times of the strongest amplitude changes. The number of dv/v measurements in the MWCS-based inversion approach quantifies the positive effect of the filter. About $4.7 \cdot 10^6$ estimates with $cc < 0.85$ were removed from the total $12.5 \cdot 10^6$ compared to the removal of $9.7 \cdot 10^6$ estimates from the unfiltered data. The consistency between the results associated with each correlation tensor component and the results obtained with a joint inversion of all data (gray and black lines, Figures 3h and 3i) implies a high degree of mixing or randomization of the wavefield, again compatible with the conclusions drawn from the stable H/V ratios in the previous section. We continue with inverted dv/v time series that we obtained from MWCS-analyzed correlation functions that have been filtered using the SVDWF.

4. Velocity Changes

4.1. The Seasonal Response

In the next section we separate the seasonal signal from the 2010 dv/v results containing the transient responses to the deep creep events. The thin light-colored lines in Figure 4 show the seasonal response for the years 2008, 2009, and 2011–2015 during the analysis window centered on the 100 days after April 4. The corresponding thick lines are the multiyear averages. Recall that the sample rate is one point per 2 days, and the averages are smoothed with a ±5-point running average. The spatial variability of the seasonal response is significant (Figures 4 and 5), with large amplitudes in the area to the west of the fault (Figure 4a) and a

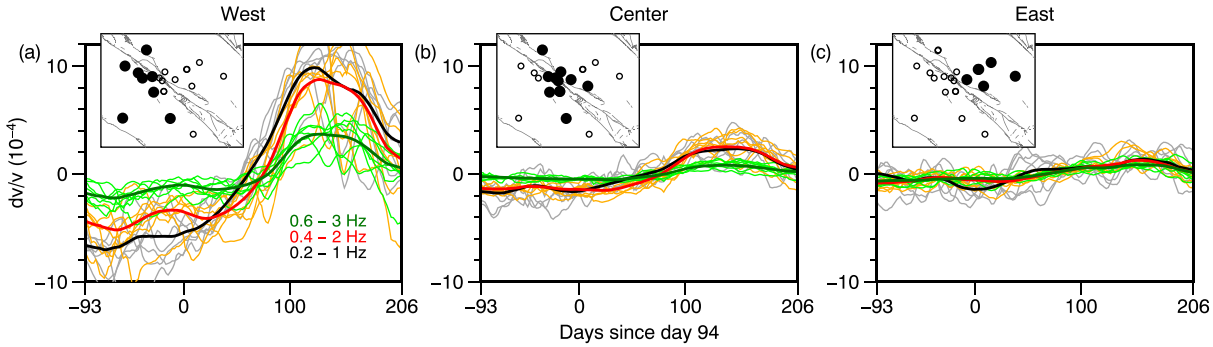

Figure 4. Frequency-dependent seasonal dv/v variability in the (a) west zone, (b) center zone, and (c) east zone. The associated group of stations is shown in the insets. Thin curves indicate the response in the years 2008, 2009, and 2011–2015. Thick curves are the corresponding multiyear averages. A lapse time window of 20–50 s is used.

weak or zero signal in the region to the east of the fault (Figure 4c). The imaging of the peak-to-peak seasonal dv/v change in the 0.3- to 1.5-Hz range shown in Figure 5 is detailed in section 5.1. These results are compatible with the view that the thermoelastic strain response dominates the seasonal response pattern in the area (Hillers, Ben-Zion, et al., 2015). The results show now in more detail that this effect likely results from the significant annual temperature changes (Hillers, Ben-Zion, et al., 2015) in combination with the structural heterogeneity across the Anza gap area. This involves strong topographic gradients in the region (Figure 1b), material and rheology contrasts across the San Jacinto fault (Allam & Ben-Zion, 2012; Fang et al., 2016; Sharp, 1967) that translate into a broadly reduced shear modulus to the west (Lindsey et al., 2014), changes in the lithology on both sides along the fault (Sharp, 1967), and perhaps also spatially variable fluid saturation as suggested by hot springs in the study area (Figure 1b). The pivotal mechanical properties of the Anza section are indicated by the seismic quiescence of the locked fault segment in that area.

The amplitude of the seasonal variation decreases with frequency (Figure 4). As detailed in section 5.2 on the depth resolution, this implies that the medium change at depth is larger. Within the thermoelastic strain hypothesis, we think of three mechanisms that can be responsible for this trend. First, thermoelastic strains generally decrease with depth. However, the wavenumber dependence of the solutions (Tsai, 2011) controls the shift of the maximum of individual directional strain components to greater depth. A dominant direction of strain could thus lead to medium changes and hence dv/v changes that peak well below the surface. The other two mechanisms consider the coupling of the thermoelastic loading with possible though typically harder to quantify fluid effects. An immediate fluid-related mechanism is the variation of the groundwater level (Clements & Denolle, 2018; Hillers et al., 2014; Sens-Schönfelder & Wegler, 2006). An alternative explanation to this wet-dry effect is the enhancement of velocity changes in overpressured or fluid-saturated areas (Brenguier et al., 2014; Duputel et al., 2009). The larger dv/v values at depth can

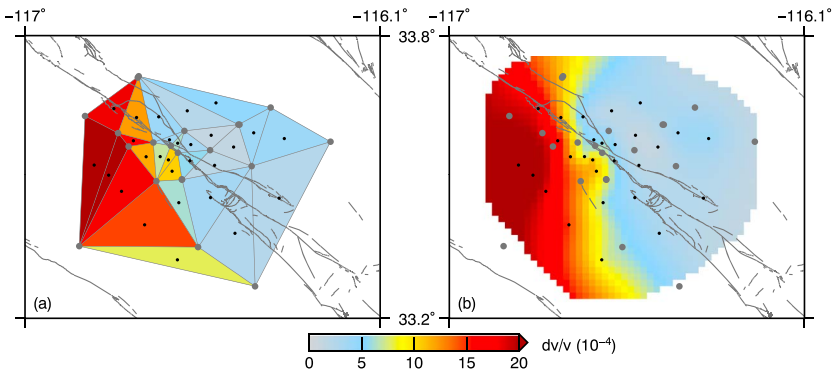

Figure 5. Spatial distribution of the peak-to-peak seasonal dv/v change obtained from the multiyear station triplet averages, 0.3–1.5 Hz, 20–50 s. Gray and black dots mark the station locations and the triangle center locations. (a) Color indicates the seasonal dv/v change estimate at the triangle center locations. (b) Spatial dv/v distribution obtained from the data in (a) using the method described in section 5.1.

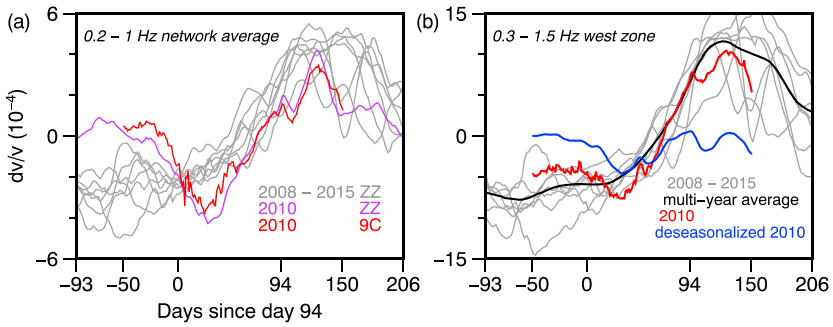

Figure 6. (a) Network average dv/v changes in the 0.2- to 1-Hz frequency range including surface and borehole station data for the years 2008, 2009, and 2011–2015 (gray). The purple line is the corresponding 2010 result. The red line is the 2010 result obtained with the nine-component correlation data. These data are similar to the surface station 0.2- to 1-Hz results in Figure 3i. (b) Same as in (a) for stations in the west zone for 0.3- to 1.5-Hz data. A lapse time window of 20–50 s is used.

possibly reflect a fluid-related increased susceptibility to deformation that can be further amplified by a sensitivity to a dominating direction of strain.

4.2. Separation of Deep Creep and Seasonal Responses

Figure 6a compares the 2010 dv/v time series containing the seasonal and the deep creep response—similar to Figure 3i—to the results from the other years that are dominated by the seasonal signal. The removal of this seasonal signal from the 2010 response is illustrated in Figure 6b. Compared to the gray-colored 2008, 2009, and 2011–2015 network averages including borehole data in Figure 6a, the 2010 curves in purple and red show a different post-t_0 dv/v behavior that we have been associating with the proposed aseismic creep transient triggered by the EMC earthquake. The dv/v inversion yields a neutral average over the analysis period, which explains the different dv/v "baseline" level in the period before day 0 in 2010 compared to the levels in the other years. The difference in the 2010 ZZ (purple) and 9C (red) curves in Figure 6a are thus only partially governed by the single-component versus nine-component data and different sampling intervals. The length of the analysis window and the resulting different averages also influence the shape of the obtained curves.

We find that the difference between the 2010 signal and the multiyear average response depends on frequency and position. The clear difference shown in Figure 6a appears at low frequencies and for the full network average. For a station subset to the west of the fault (Figure 6b), the seasonal signal is significantly above average and thus also dominates the 2010 response, so that the 2010 values are generally within the range of values obtained in other years. In all cases, however, the downward slope of the 2010 transient onset is opposite to the upward showing trend of the average seasonal effect at this time of the year, which also serves as a discriminator.

We remove the seasonal trend from the target deep creep response signal by subtracting the ZZ low-resolution multiyear average (black line in Figure 6b) from the 9C high-resolution 2010 data (red line). Time series discussed in Figures 7 and 10d correspond to the resulting blue indicated deseasonalized data in Figure 6b. The high similarity between the ZZ and 9C results (Figure 3i) allows us to take the ZZ data as proxy for the seasonal behavior. Before subtraction, we first scale and shift the multiyear average curve to match the 2010 seasonal low- and high-amplitude difference and the 2010 baseline level at $t < 0$ days. While the 2010 results are relatively similar to the average seasonal signal at $t > 50$ days, the neutral-average effect makes it more difficult to study details of the response at $t < 0$ days. We varied the amplitude and level of the subtracted seasonal response to minimize the discrepancy in this period. However, the overall evolution and shape of the resulting response pattern is not much affected using different scaling strategies, in particular at $t > 0$ days, but the pre-t_0 level remains somewhat arbitrary. We set the zero level as the average of the values from before the EMC event, between the EMC and Collins Valley event responses, and after the Collins Valley event related signals, that is, from $t < 0$, $75 < t < 90$, and $t > 125$ days.

We point out that wavefield changes also contribute to the difficulty of optimally constraining the behavior around the transient onset. Figure 2c shows systematically below-average energy values in the 20 days before the EMC earthquake. The H/V marker in Figure 2d exhibits significant fluctuations in the 10 days before the

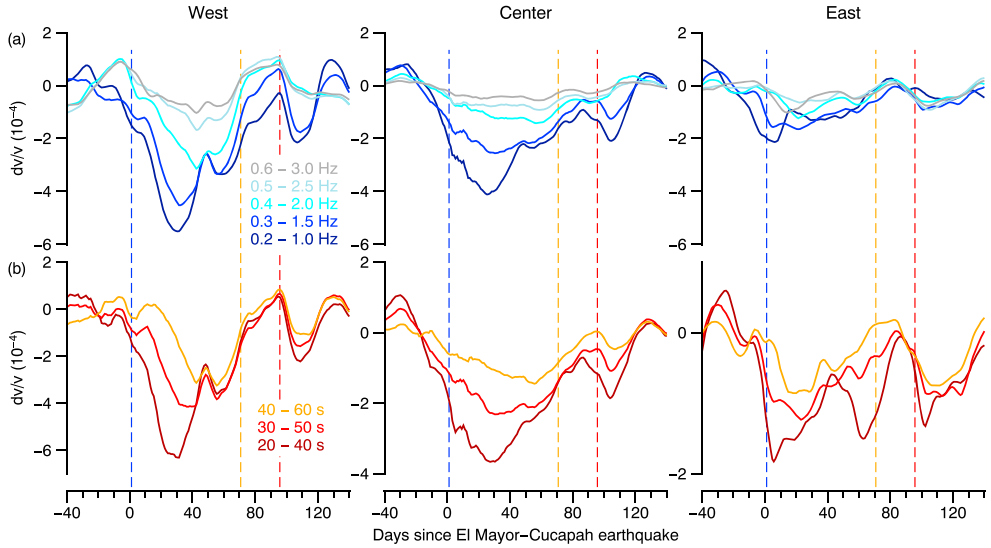

Figure 7. (a) Frequency-dependent and (b) lapse time-dependent evolution of the dv/v changes for the three west, center, and east zones indicated in Figure 4. The lapse time window for the results in (a) is 20–50 s. The frequency range used in (b) is 0.3–1.5 Hz. The vertical lines indicate the occurrence of the correspondingly colored events in Figure 1a. The daily sampled time series are smoothed with a ±1-point running average.

event, in particular in the 0.8- to 1.6-Hz frequency band. Importantly, the orange line in Figure 3g highlights that the contribution to the dv/v inversion from the ~25 days before and after t_0 is relatively low, where the effect at $t > t_0$ is controlled by the aftershock activity (section 3.1). This means the dv/v results in the time period around the onset of the deep creep event are less well constrained. The downward slope beginning prior to t_0 in the 2010 results in Figures 6a and 6b and in some of the dv/v curves shown in Figures 7 and 10d thus do not indicate a precursor signal but are overall less well constrained because of the poorer data quality in the 50–60 days around t_0.

4.3. Frequency, Lapse Time, and Regional Dependence of the Transient Changes

The zonation reveals a significantly more detailed picture compared to the network averages discussed in the quality assessment in section 3. The division into a west, center, and east zone (Figures 4 and 7) is based on the similarity or zero-lag correlation coefficient between the underlying 150-day-long 2010 dv/v time series obtained from station pairs or triplets in each zone. We compute the dv/v curves for five frequency bands between 0.2–1 and 0.6–3 Hz (Figure 7a) using the same 20- to 50-s coda window as in the broadband 0.2- to 2-Hz quality assessment. Results in the 0.1- to 5-Hz range (not shown) are compatible with the 0.2- to 1-Hz results but are characterized by significant fluctuations, even if we adapt the processing parameters to the longer wave periods and longer convergence timescales. We combine data from the surface and the borehole sensors for all but the 0.2- to 1-Hz results, where the borehole data become too noisy. Above this range we do not find systematic differences in the dv/v responses from the deconvolved 2-Hz borehole sensor data and the surface stations. For the 0.3- to 1.5-Hz (Figure 7b) and the 0.5- to 2.5-Hz range we compute the responses in three lapse time windows of 20–40, 30–50, and 40–60 s.

Similar to the seasonal response pattern, peak dv/v amplitudes after the EMC earthquake are largest in the west zone and decrease across the fault toward the east zone (Figure 7a). The inverse frequency dependence of the transient dv/v amplitude change, and the implications of the timing of the frequency-dependent peak velocity changes in the west and center zones are discussed in section 5.2. The transient duration is about 70–90 days. The signals in the west zone show a clear change in the slope of the relaxation at the time of the two successive M4.9 and M4.2 events that occurred 70 days after the EMC event on the San Jacinto fault (Figure 1). We verified the "positive kink" around $t = 50$ days in the west zone using multiple other zonation and averaging strategies. The weak east zone response appears relatively independent of frequency above 0.3 Hz, and the minimum at t_0+20 days is reached earlier compared to the west and center zone results.

The main features in the coda lapse time τ patterns (Figure 7b) are the inverse τ-dependent scaling of the maximum reductions—later windows, smaller peak amplitude—and the correlation with the peak

timing—later windows, later peak timing. All these dependencies are also observed for the 0.5- to 2.5-Hz results. In the multiple scattering regime associated with longer lapse times potential source effects are reduced and the change estimates better reflect the medium response. The late-coda results are thus an additional strong indicator that the dv/v variations reflect the medium changes induced by aseismic fault motion at depth, which is further discussed in section 5.2.

The response associated with the Collins Valley earthquake at $t = 94$ days is clearly visible in all results. Compared to the post-EMC event results the dv/v reductions are smaller and the transient duration is shorter. Similar to the EMC event-related observations the velocity reductions in the west and center zones are larger at low frequencies, and the lapse time dependence is also consistent. Note that the time series in Figure 7 are smoothed with a three-point moving average for better legibility, but we verified that the velocity drop is gradual and not abrupt, as can also be inferred from the timing of the peak about 15 days after the event.

As discussed in section 4.2 on signal separation, the different neutral averages controlled by the different relative velocity states in the 2010 and the multiyear dv/v averages, and the poorer data quality around t_0 contribute together to the pre-t_0 fluctuations seen in Figure 7. From our analysis we are nevertheless confident that the data quality supports the conclusion of resolving a gradual onset of the velocity change transient at or shortly after t_0, in contrast to the alternative scenario of an instantaneous drop in dv/v at t_0. The pre-t_0 fluctuations on the 10-day scale that are not eliminated or muted by the filter decrease with frequency and lapse time. This means they decrease as a result of the better wavefield randomization through scattering that tends so reduce signatures of the noise excitation that is related to environmental triggers, changing atmospheric and ocean state patterns, and anthropogenic activity. The onset of the Collins Valley event response, however, is better resolved compared to the EMC event response. This is due to the much better alignment of the 2010 and the average multiyear response around $t = 100$ days (Figure 6b), which allows a cleaner signal separation.

5. Constraining the Spatial Distribution

5.1. Regionalization of the Time-Dependent Response

Imaging the lateral distribution of velocity changes is based on the inversion of pairwise dv/v estimates from all station combinations using statistical end-member models for the scattered energy propagation (e.g., Obermann et al., 2014). We tested this approach but found that the inversion results were unstable due to fluctuations in the underlying dv/v time series from the pairwise 9C data. The ambiguous definition of the reference and pre-t_0 level in the deseasoning step, which is also essential for spatially consistent dv/v variation patterns, contributes to these problems. We found that data from more than two stations have to be averaged to arrive at sufficiently stable dv/v time series similar to those shown in Figures 3, 4, 6, and 7. We expect that the filtering or decomposition (Hobiger et al., 2012; Richter et al., 2014; Wang et al., 2017) of daily sampled multiyear time series supports more stable spatial inversions.

We adopt a simpler imaging approach based on regionalization (Brenguier et al., 2008, 2014; Hobiger et al., 2014). We found that a triangulation-based zoning sufficiently trades off stacking or averaging—using 3 times more data compared to the pairwise approach—and spatial confinement. For this we estimate dv/v values by averaging data from three-station configurations—triplets—that are associated with all nonoverlapping station triangles (Figure 5a). For each of these triplets or triangles we subtract the low-resolution seasonal average from the high-resolution 2010 dv/v time series. For quality assessment, dv/v values of each triplet are associated with the number of daily correlation pairs with $cc \geqq 0.85$ that entered the dv/v inversion scheme ($O(10^5) - O(10^6)$). These are scaled to triplet-specific weights between zero and unity. These weights scale with the average interstation distance. We then map the dv/v value to the center position of the associated station triangle. The dv/v value can be the seasonal peak-to-peak amplitude (Figure 5), the estimate at any given day during the study period (Figure 8), or the maximum dv/v reduction during the EMC event response (Figure 9a).

There are three sites with colocated surface and borehole stations (Figure 1b). The associated triangle estimates can thus be built from two or more station triplets. We compute weighted dv/v averages at the center locations of those triangles that contain colocated stations. The resulting dv/v estimate associated with each triangle is shown in Figure 5a for the seasonal peak-to-peak amplitude distribution. Finally, we estimate a 2-D distribution (Figure 5b) from the weighted values at the center locations using the *surface* function from The Generic Mapping Tools (Wessel et al., 2013). The imaging area is defined by the envelope around

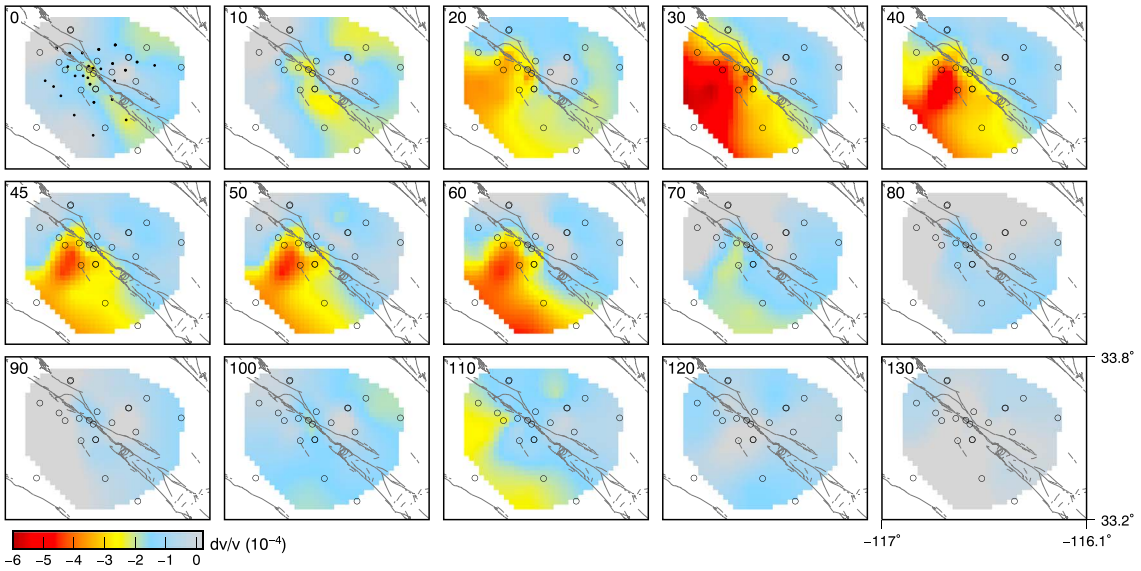

Figure 8. Temporal evolution of the dv/v change pattern obtained from station-triplet results, 0.3–1.5 Hz, 20–50 s. Numbers in the upper left denote days since the El Mayor-Cucapah event. Circles mark station locations. Dots in the first frame indicate triangle center locations.

10-km circles around the triangle center locations. A tension factor in the 0–1 range controls the scale of the variations, similar to the tuning parameters in the pairwise least squares inversions (Obermann et al., 2014) that are used to trade off model variance and misfit. The chosen value of 0.2 yields the distributions shown in Figures 5b, 8, and 9a. It resolves variations on scales that we think are supported by the network geometry and interstation distances. The main features and results are not sensitive to reasonable changes of the tension factor.

The scattered wave propagation models—also referred to as sensitivity kernels—used in the inversions of spatially variable dv/v estimates imply that the largest sensitivity to medium changes is at the station location itself (Pacheco & Snieder, 2005). This is why the more recent implementations of the simpler regionalization strategies (Brenguier et al., 2014; Hobiger et al., 2014) use station locations and not in-between locations as reference points. At least the study of Brenguier et al. (2014), however, benefitted from a dense, regular network for this task. We also test this idea and compute dv/v time series using correlations between every "master" station and its five nearest neighbors. We exclude connections between neighbor stations to emphasize the association of the obtained velocity changes with the master location. All other processing steps are the same as in the triangulation approach. The resulting peak-to-peak seasonal amplitude distributions (not shown) are very similar compared to the triangle approach. The key features of the dv/v response following the 2010 EMC event are also compatible considering the different positions of the triangle centers and the station locations and thus support our conclusions. The two distributions obtained with the master station and the triangle approach differ most significantly to the north of the Anza gap and to east of the fault, in the region between the KNW station and the PMD and PFO stations (Figure 1b). The master station approach puts significantly decreased amplitudes in this area, similar to those on the southwest side of the fault, therefore creating a more fault symmetric pattern compared to the triangle-based results that have overall neutral values in this area (Figure 8). The master approach, however, does not include connections across this area between the KNW and PFO sites, and the five nearest-neighbor pairs cover only a limited azimuthal range. The large KNW amplitudes governed by the connections to the south across the fault are thus interpolated to the east. Because of the explicit delimitation of the triangles, we favor the associated triplet results. It has also the appeal of yielding 43 instead of 21 different values before the weighted averaging is applied.

The space-time evolution obtained from the 0.3- to 1.5-Hz, 20- to 50-s results (Figure 8) show that velocities decrease first along the fault. The transient following the EMC event lasts for 65–70 days, and the maximum reduction occurs around 30 days after the event to the southwest of the fault, within the Anza gap. The transient reduction is modulated by a clearly resolved intermittent recovery period around 45 days—the above mentioned "kink" in Figure 7. Velocity variations are smallest to the northeast of the fault

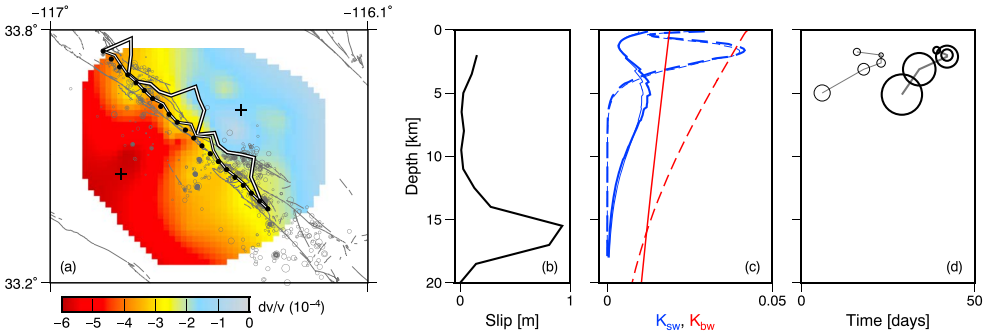

Figure 9. (a) Spatial distribution of the maximum dv/v reduction during the 80 days after the El Mayor-Cucapah (EMC) earthquake. Gray lines indicate mapped faults. Gray circles show seismicity in the 80 days after the EMC earthquake. Crosses denote the sites for which the K_{sw} kernels in (c) have been estimated. Black dots indicate the fault parametrization of Inbal et al. (2017). The black-and-white lines show the cumulative slip distribution of the post-EMC creep event in two depth sections along this track. The line with larger (smaller) amplitudes corresponds to slip below (above) 8-km depth. (b) Cumulative slip distribution along the Anza seismic gap section (along grid point 5 from the NW to 12 in (a)). (c) Blue lines are Rayleigh wave kernels K_{sw} from the two sites to the west and east of the fault for two frequencies. Thick (thin) lines indicate data from the west (east). The red lines are the body wave kernels K_{bw}/τ with units 1/km for the whole region. The solid (dashed) lines correspond to the low-frequency (high-frequency) solutions. For K_{sw}: $f = 0.2$ Hz and $f = 0.6$ Hz. For K_{bw}: $l^* = 50$ km and $l^* = 10$ km. K_{sw} and K_{bw} are on the same scale. (d) Circles indicate the timing of the peak dv/v reduction in the areas to the west (thick lines) and east (thin lines) of the fault (from Figure 7). Circle size is proportional to the dv/v amplitude. The vertical position of a circle is associated with the K_{sw} kernel peak of the lower bound of the frequency range.

in the area between the fault and the PFO site. The region that exhibits the maximum seismic velocity changes 30 to 60 days after the EMC event shows within the location uncertainties at day 110 a remarkable gap in the maximum velocity change associated with the Collins Valley event. This can potentially be associated with evolving material properties in response to the inferred successive loading episodes. However, this triangulation-based detail should be verified in future analyses using updated pairwise-based inversion results.

5.2. Estimating the Depth Resolution

Estimating the depth of the medium changes is crucial for constraining the underlying source properties. For scattered wave propagation, the velocity structure and thus the surface wave sensitivity (Figure 9c, blue) together with the medium heterogeneity are the two main properties that control the resolvable depth regime of the medium changes, and the time, frequency, and lapse time-dependent dv/v observations in Figure 7. At lapse times up to 8 times the transport mean free time t^* the coda wave sensitivity is dominated by surface wave properties (Obermann et al., 2016). Later, body waves dominate. The time t^* is proportional to the inverse frequency f-dependent transport mean free path l^*, $t^* = l^*/c_E$, where c_E is an effective energy velocity. Depth-dependent body wave sensitivity kernels (Figure 9c, red) can be computed using analytical solutions of scattered energy propagation (Pacheco & Snieder, 2005) that depend on τ and the diffusion constant $D = l^* c_E/3$; c_E depends on the energy ratio of S waves and P waves at the surface. Here we use $1/c_E = 0.89/v_S + 0.11/v_P$ based on a ratio obtained with numerical simulations of wave propagation in an attenuation-free 3-D heterogeneous elastic medium (Obermann et al., 2016).

It follows that the dv/v value estimated at a given frequency f and lapse time τ in the coda is governed by the $\tau/t^*(f)$ controlled partitioning α, the f-dependent depth resolution of the surface waves involved, and the τ and $l^*(f)$-dependent body wave sensitivity. These connections can be used to invert τ and f-dependent dv/v estimates for the lateral and vertical position of the actual velocity changes in the medium $\Delta v/v$ (Obermann et al., 2019), understanding that $dv/v \propto \alpha(dv/v)_{sw} + (1-\alpha)(dv/v)_{bw}$. The $(dv/v)_{\langle\cdot\rangle}$ estimates based on surface waves (sw) and body waves (bw) depend on the respective kernels $K_{\langle\cdot\rangle}$ via $(dv/v)_{\langle\cdot\rangle} \propto K_{\langle\cdot\rangle}/\tau \cdot \Delta v/v \cdot \Delta V$, where $\Delta v/v$ is again the local variation in a voxel ΔV. However, as even solutions to the simpler lateral 2-D problem have to await cleaner dv/v estimates (section 5.1), we focus here on a discussion of the dominating regimes to evaluate the implications of the f dependence of the seasonal and postearthquake dv/v amplitude pattern, the f dependence of the timing of the peak velocity change, and the τ dependence of the amplitude pattern and the peak timing.

Hillers et al. (2013) parametrized the lateral heterogeneity in the study area from the tomographic model of Allam and Ben-Zion (2012) and estimated scattering angle-dependent 20 km $< l <$ 150 km for 0.5-Hz Rayleigh waves. Anache-Ménier et al. (2009) estimated l in the 1- to 10-km range for 5- to 7-Hz body waves in the PFO area. The ratio of l and l^* depends on the scattering anisotropy. Clearly, the length scale l^* after which all information about the original direction of propagation is lost is larger than the average distance l between two scattering events. Typical ratios for anisotropic scattering are around 1.5. For the body wave kernels in Figure 9c we thus use $l^* = 50$ km for the lower and $l^* = 10$ km for the upper frequency range and an effective velocity $c_E = 3.6$ km/s. The associated low- and high-frequency mean free times are thus around 14 and 3 s, and the typical wavelengths associated with c_E (Obermann et al., 2016) are in the 12- and 2-km range, respectively. For a window average lapse time of 35 s this results in τ/t^* ratios of 2.5 and 13, which suggests the coda at low and high frequencies is dominated by surface waves and body waves, respectively.

The frequency- and depth-dependent surface wave kernels $K_{sw} = \partial c/\partial v_S$ in Figure 9c (Herrmann, 2013) are based on profiles from the tomographic velocity model of Fang et al. (2016). They indicate Rayleigh wave sensitivity above the proposed deep creep zone at 15-km depth (Figure 9b), and for most of the used frequencies the sensitivity is above 5–8 km. We assume here that the wide frequency ranges are dominated by the low-frequency content considering the frequency-dependent decrease in coherency on the flank of the microseisms peak and the faster attenuation of waves with shorter period. Alternatively, the surface wave sensitivity vanishes at depths larger than two thirds of the typical wavelength (Obermann et al., 2016), which yields very similar estimates. The low-frequency kernels from around the PFO area in Figure 9c, the data in the east zone, imply a 20% smaller peak sensitivity compared to the $K_{sw}(z)$ values estimated in the area to the west of the fault. The otherwise similar depth resolution suggests that the laterally different dv/v amplitudes and time histories are not governed by processes or effects in different depth ranges.

We use a 3-D sensitivity kernel for coincident source and receiver assuming body wave energy propagation can be modeled as a diffusion process (Pacheco & Snieder, 2005). At a given depth the 3-D kernel is integrated over the horizontal domain to yield $K_{bw}(z, \tau)$ and normalized by τ to ensure $\int K_{bw} dz = 1$ (Hillers et al., 2014; Sens-Schönfelder & Wegler, 2011). The kernels for $l^* = 50$ km and $l^* = 10$ km, proxies for the low- and high-frequency regime, suggest that the scattered body waves can probe the medium response in the depth regime of the proposed creep event, whereas the surface wave sensitivity is constrained to the region above 10-km depth. Note, however, that the surface wave depth integral $\int K_{sw} dz$ is on the order of 0.1, that is, the body wave sensitivity in Figure 9c appears exaggerated relative to the surface wave sensitivity.

For the assessment of the frequency and lapse time patterns we focus on the high-SNR dv/v results obtained in the west and center zones. We begin with the inverse frequency-dependent change of the dv/v amplitude. At the low frequencies for which $\tau < 8t^*$ and hence surface waves dominate, the decreasing K_{sw} values with depth for longer periods (Figure 9c) suggest together with the inverse frequency dependence of the measured dv/v values that the medium change $\Delta v/v$ is larger at depth. The continuation of this trend into the regime that is dominated by body waves is compatible with the frequency-dependent properties of the body wave kernels, because K_{bw} values at depths at and above the suggested slip zone at 15 km (Figure 9b) decrease, too, with decreasing frequency due to the increasing scattering length scale. Another change-in-regime-related factor that contributes to the decreasing dv/v changes is the overall smaller body wave sensitivity (Obermann et al., 2013) considering the $\int K dz$ scaling. The dv/v frequency patterns and the properties of surface and body waves imply thus that the medium change and hence also the deformation at depth is larger compared to the near-surface layers. This behavior holds for the seasonal loading (section 4.1 and Figure 4) and the proposed deep creep response (Figure 7a).

Next we assess the frequency-dependent timing of the maximum or peak dv/v reduction. Combining the inverse frequency-dependent depth scaling of the velocity changes with the timing of the peak dv/v reduction (Figures 7a and 9d), we infer a delayed arrival of the maximum medium change toward shallower depths. This suggests an upward migration of the medium deformation. An extrapolation of this pattern toward greater depth is compatible with the deep slip hypothesis. We emphasize the reverse trend at higher frequencies indicated at shallower depths. The smaller circles associated with higher frequencies in Figure 9d tend to indicate smaller delay times. This is perfectly compatible with the notion that the two highest frequency bands are dominated by body waves that sample the deeper parts where the deformation arrives earlier. The shallow location of the circles that follows the surface wave kernels had thus to be modified considering the partitioning of surface and body wave sensitivity. We iterate that the late

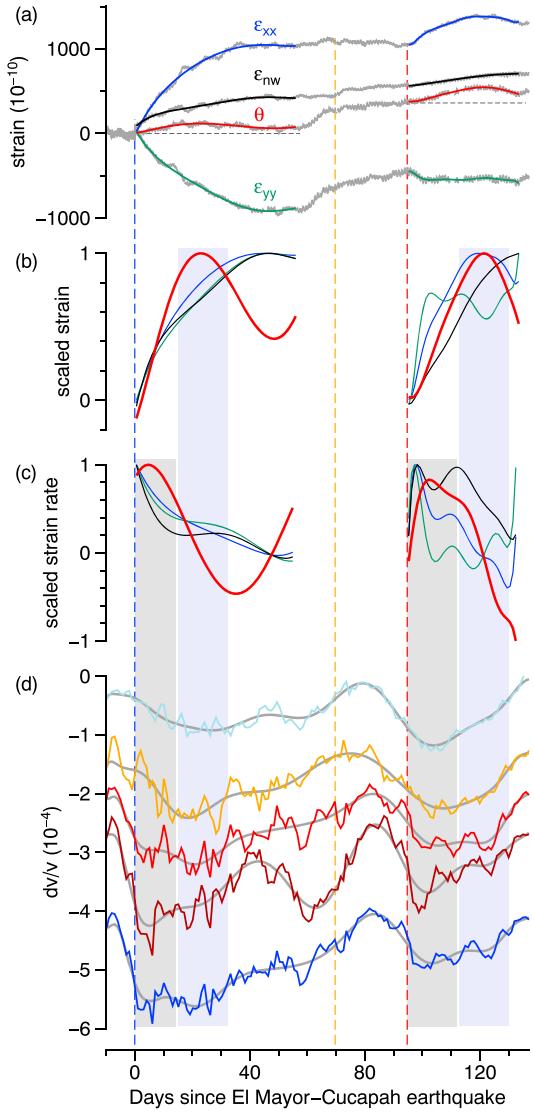

Figure 10. (a) Records from the Piñon Flat Observatory laser strainmeter (gray). Colored line segments are fitted polynomials. $\varepsilon_{\langle\cdot\rangle}$ indicates horizontal strain components, and θ denotes volumetric strain. (b) Normalized fits to the data in (a). (c) Differentiated and normalized data from (b). (d) Relative velocity change data from Figure 7. Colored lines are the daily resolved dv/v curves, and the gray lines are polynomial fits to illustrate trends. Colors are the same as in Figure 7. Light blue: 0.5–2.5 Hz, 20–50 s; orange: 0.3–1.5 Hz, 40–60 s; red: 30–50 s; dark red: 20–40 s; blue: 20–50 s. All data are from the east zone and on the same scale but offset for clarity. Vertical lines indicate the occurrence of the correspondingly colored earthquakes in Figure 1a. Gray and light blue patches indicate periods associated with peak strain rate and peak strain.

lapse time results confirm the spatially variable seismic velocity reduction in the Anza gap area following the EMC and Collins Valley events. The lapse time-dependent dv/v reduction and delayed peak timing in Figure 7b appears to be governed by properties of the surface wavefield considering that τ/t^* ratios for the three considered τ windows in the low-frequency regime are in the range 2–4. In this case, we attribute the τ dependence to lateral averaging effects (Obermann et al., 2016). The decreasing dv/v amplitude data can also be influenced by an increasing body wave partition due to the smaller kernel values. A body wave dominance $\tau/t^* > 8$ for this lapse time and period range requires l^* to be not larger than 20 km. Although this scenario cannot be ruled out considering the uncertainties in the l estimates and l/l^* relation, a body wave dominance is not expected because a reversed trend in the dv/v peak timing is not observed.

6. Strain Observations

We compare records from the long base laser strainmeter at the PFO site (Figures 10a–10c) to the dv/v time series from the colocated east zone (Figure 10d). The records of the N-S, E-W, and NW-SE strain components (Figure 1b), ε_{yy}, ε_{xx}, ε_{nw}, are hourly sampled. Tidal components are removed. Twenty-four-hour averages yield time series that are sampled at the same daily resolution as the dv/v data. Volumetric strain $\theta = \varepsilon_{xx} + \varepsilon_{yy} + \varepsilon_{zz}$ is estimated from $\varepsilon_{zz} = \xi(\varepsilon_{xx} + \varepsilon_{yy})$ at the surface of a traction free half-space, where $\xi = -\nu(1-\nu) = -1/3$, and $\nu = 1/4$ is Poisson's ratio.

Figure 10a shows in gray the hourly sampled strain data in relation to the 40-day average before the EMC event. Positive values correspond to extension; that is, proposed right lateral slow slip on the ~130° trending fault yields large extensional strains in the E-W direction, large compressional strains in the N-S direction, and a smaller extension signal on the NW-SE component (Figure 1b). We compare the dv/v time series to the strain data and strain rate estimates (Rivet et al., 2011). For clean estimates we limit the analysis to 55- and 40-day-long time windows that end after the occurrence of the peak strain amplitudes following the two earthquakes. The 55-day range after the EMC event stops just before the emergent onset in the ε_{yy} and θ data (Figure 10a). This excursion seen on one strainmeter at $t = 56$ days has been traced to an instrumental problem. We then fit a fifth-order polynomial to these daily sampled strain data segments. These are the colored line segments in Figure 10a. Strain rate is obtained by differentiating these functions. The choice of the order 5 is not important for our conclusions. Figures 10b and 10c show the scaled absolute values of the obtained strain and strain rate functions. Strain on the individual components is maximum shortly before the end of the considered 55-day range after the EMC event. In contrast, volumetric strain peaks 30 days earlier due to the different ε_{xx} and ε_{yy} behavior and the opposite signs.

The dv/v time series in Figure 10d are the results for the 0.3- to 1.5-Hz (bottom, blue line) and the 0.5- to 2.5-Hz (top, light blue line) ranges using the 20- to 50-s window, and the lapse time-dependent 0.3- to 1.5-Hz results (20- to 40-s dark red line to 40- to 60-s orange line). The data and the colors correspond to the Figure 7 east zone results. Recall that the data in Figure 7 have been smoothed. In Figure 10 we show the original data from the east zone to highlight the daily resolution of the time series. The low-pass time series shown in grey—again a polynomial fit using the same order 5 as for the strain analysis—should facilitate the comparison with the strain data. We emphasize that these east zone dv/v results are characterized by lower signal amplitudes and thus a lower SNR compared to the west zone results (Figure 7).

The principal robust observation from the comparison of strain data (Figure 10a) and the associated dv/v time series from the east zone (Figure 10d) is that two deformation episodes correspond to the proposed deep creep transients. In both cases the positive θ changes indicate volumetric extension that are associated with a reduction in seismic velocities followed by a recovery. That is, the timing and the mechanism are consistent across the sequence. This notion is supported by the similar behavior in the west zone, where, as we repeatedly remarked, the higher SNR reflects the larger susceptibility in that area compared to the east zone. We point again out that we do not associate the decreasing trend before t_0 in the dv/v time series in Figure 10d with a precursor signal, but with poor resolution caused by fluctuations in the ambient wavefield properties (section 4.2). In conclusion, the consistency between strain and velocity change signals advocates joint analyses of the two data types for improved detection capabilities and for improved monitoring and better resolution of slip episodes in active fault zone regions.

To determine further whether peak velocity reductions correspond better to the volumetric strain or the strain rate functions, we indicate time windows around the maxima in the respective strain signals across Figures 10b–10d using light blue and gray patches, respectively. The results differ for the two responses. The maximum velocity reductions following the EMC earthquake fall mostly inside the peak volumetric strain range (blue patch). The exception to this rule is the dark red colored low frequency, early lapse time curve, where the minimum shows a better correlation with the strain rate. Note that the lapse time-dependent delay in the timing of the peak reduction is consistent with the observations from the west and center zones discussed in section 5.2.

The results associated with the Collins Valley event are clearer. Here, too, we discern a slight shift in the peak time with τ. However, all obtained velocity change curves have a minimum early after the earthquake and the assumed onset of the deep creep event and correlate thus systematically better with the period of high strain rate in the first 15 days. The clear upward trajectories of most curves indicate a recovery process during the light blue high-volumetric strain period around 30 days after the earthquake, which suggests a decreased sensitivity to this deformation mode compared to the preceding EMC event response.

7. Discussion

Using ambient seismic noise data, we resolve transient seismic velocity changes in the region around the Anza seismic gap in the central section of the SJFZ. These changes coincide with signals recorded on the long base laser strainmeter at the PFO. Analysis of wavefield and correlation quality markers indicate that the observed dv/v variations in the 70 and 30 days following the EMC and Collins Valley earthquakes are not governed by aftershock-induced changes in the seismic noise properties. Constraints on the lateral velocity change distribution are provided by the triangulation approach. The most striking observation is the significantly different response in the area to the west of the fault compared to the area to the east between the fault and the high plateau hosting the PFO strainmeter. The overall consistency of the dv/v change patterns in response to seasonal loading and to the proposed creep episodes highlights the distinct behavior of the batholith hosting the PFO site and the importance of the structural variations across the Anza seismic gap region. We discuss the implications of the relevant tomographic images in more detail below.

The velocity change episodes are overall compatible with the earthquake interaction scenario proposed by Inbal et al. (2017) based on strain data from six PBO stations and local seismicity patterns. According to this scenario the EMC earthquake triggered aseismic slip on the San Jacinto fault near Anza. Data from the first 10 days after the EMC event constrained the triggered aseismic slip primarily to depths larger than 10 km. The accumulated slip corresponds to a moment magnitude of 5.9. The associated stressing of the surrounding fault segments is thought to have contributed to the nucleation of the Collins Valley event, which triggered another aseismic slip episode with moment magnitude 5.8. The microseismicity that was used to constrain properties of the deep creep events was assumed to occur on the primary San Jacinto fault interface. Follow-up work indicates that small events in the area nucleate primarily off-fault while moderate and large events involve slip on the main faults that tend to dip to the northeast below ~10-km depth (Cheng et al., 2018; Ross et al., 2017; Trugman & Shearer, 2017). The distribution of the microseismicity in broad damage zones also likely explains the scarcity of repeating events (Jiang & Fialko, 2016) that occur on asperities situated in creeping regions along more mature fault zone segments such as the central San Andreas fault (Khoshmanesh et al., 2015). Approximating the volumetric deformation processes to occur on a single plane may lead to erroneous inferences concerning the duration, size, or position of the slip events. In any case,

the existence of tens-of-days-long deformation episodes in the focus area following the EMC and the Collins Valley earthquakes is substantially supported by the consistency of our seismic observations and the strain signals at PFO and the PBO stations (Inbal et al., 2017). We thus continue to work with the hypothesis that the observed dv/v variations reflect the spatiotemporal medium response to creep episodes.

Inbal et al. (2017) inferred three main creep patches on the San Jacinto fault in response to the EMC event. These are visible from the along-fault amplitude distributions in Figure 9a that are separated in a shallow (<8 km) and deep (>8 km) average. The coincidence of the obtained dv/v pattern to the west of the fault and the deep profile characterized by the larger amplitudes is highlighted by the compatibility of the along-strike position of the maximum velocity reduction with the position of the largest slip at depth. Faint shallow creep is confined to a small region in the center. Nevertheless, the distribution of these small amplitudes along the seismic gap section coincides with the position of red dv/v areas next to the fault. These relations are another strong indicator of a causal relationship between the obtained velocity change and the proposed creep phenomena. Evidence in favor of the significance of deep over shallow slip is compatible with the overall absence of shallow creep on the Anza section (Lindsey et al., 2014). This is again in contrast to the behavior of segments along more mature faults such as the San Andreas fault (Khoshmanesh et al., 2015), the North Anatolian fault (Rousset et al., 2016), or the Haiyuan fault (Jolivet et al., 2015) that all exhibit shallow creep.

The duration and amplitude of the velocity change associated with the proposed creep event triggered by the Collins Valley earthquake (Figure 8) are significantly shorter and smaller compared to the changes after the EMC earthquake, although the cumulative moment magnitudes and the slip patch locations and sizes are overall similar (Inbal et al., 2017). The different dv/v patterns suggest an evolution of the material properties in response to successive deformation episodes.

Relating the spatial velocity change distributions to the tomographic images of seismic velocities or velocity ratios obtained by Allam and Ben-Zion (2012), Fang et al. (2016), or Zigone et al. (2015) is complicated by the depth variations of the imaged properties. Are the lateral dv/v variations shown in Figures 5, 8, and 9a controlled by the response at depths above 10 km where the sensitivity is largest, or by the material properties below 10 km around the proposed deep creep regions? A visual comparison of our velocity change patterns and the images by Fang et al. (2016) reveals that the region of the largest dv/v amplitudes to the west of the fault coincides with an area of reduced v_P that is bound by material with larger velocities in the fault-parallel northwest direction. This pattern on the west side of the fault is seen over the entire 3- to 16-km-depth range. Systematically more competent material to the east that correlates with the clear change in the response across the seismic gap can only be inferred in the top 7 km from the tomographic images (Fang et al., 2016). The fault-normal profile 6 of Allam and Ben-Zion (2012) at the seismic gap indicates high (low) v_P/v_S ratios to the west (east) of the fault in the top 5–7 km. The indicated mechanical differences can also contribute to the observed variations, linking relatively smaller shear wave speeds to an increased susceptibility. These conclusions are supported by the coincidence of the fault perpendicular shear modulus μ distribution across the Anza segment that Lindsey et al. (2014, their Figure 3a) compiled from the tomographic model of Allam and Ben-Zion (2012). It shows systematically reduced values of μ to the west of the fault in the top 5–10 km where we observe the largest negative dv/v amplitudes. Similarly intriguing is the spatial relation of the PFO area where dv/v signals are smallest with a high-μ region that reaches the surface some 5 km to the east of the fault. Recall that the implied smaller in situ $\Delta v/v$ values at depth to the east are sensed by low-frequency surface waves that are characterized by a 20% smaller sensitivity K_{sw} in this area (Figure 9c). This also contributes to the resolved smaller dv/v values.

The μ profile of Lindsey et al. (2014) indicates an extensive compliant fault damage zone with reduced elastic shear modulus 5–10 km deep and 2 km around the fault that is consistent with trapped waves observations in the area (Li & Vernon, 2001; Lewis et al., 2005). Our estimated position of the maximum dv/v changes shown in Figures 4, 5, 7, 8, and 9a that is away from the densely instrumented zone around the fault supports the notion that the observations are not dominated by shallow damage zone processes. In summary, these observations provide a direct comparison between regional tomographic images, inferred variations in the rock type and competence, and velocity change amplitudes.

We discussed the depth dependence of the seasonal signal considering the possible role of fluids in section 4.2 where we referred to the significantly above-average velocity changes after the 2011 Tohoku earthquake in highly susceptible volcanic regions across Japan (Brenguier et al., 2014). Again, the existence of hot springs

in the study area (Figure 1b) implies the possibility that the low μ values and the high susceptibility leading to the observed large dv/v amplitudes in the region between the San Jacinto and the Elsinore fault are associated with elevated fluid saturation.

The dv/v results for several years show that the transients in 2010 are not governed by some systematic annually repeating environmental effect. Considering the large seasonal variation, the filter employed (Moreau et al., 2017) and the MWCS-based inversion approach (Brenguier et al., 2014) are crucial for the resolution of the transient signals in 2010. This focus on resolution comes at the cost of outstripping the available resources for the computation of equivalent multiyear time series for potentially better filtering, fitting, or decomposition (Hobiger et al., 2012; Wang et al., 2017).

A comparison of PFO strainmeter and east zone dv/v data (Figure 10) reveals a sequence of volumetric extension transients following the EMC and the Collins Valley events that correlate with episodes of reduced seismic velocities. Maximum velocity reductions after the Collins Valley event coincide better with peak strain rates compared to periods of elevated strain. The behavior following the EMC event is more ambiguous which is likely related to the fluctuations that bias the resolution of the transient onset. The strain rate-related observations are compatible with the seismic velocity change pattern in the middle crust induced by the 2006 M7.5 slow slip event on the Guerrero segment of the Mexican subduction zone (Rivet et al., 2011), where the dv/v signal also closely follows the inferred strain rate. The compatibility of the PFO strain rate signals and the dv/v observations in the east zone suggests that nonlinear failure and recovery mechanisms play a role in the observed behavior (Johnson & Jia, 2005; Lyakhovsky et al., 2009).

Overall, the consistent timing of proposed creep events, extensional strain, and reduced seismic velocities demonstrate the feasibility of seismic velocity monitoring along a hazardous fault segment to complement seismicity and geodetic observation techniques for improved resolution of the fault slip and deformation spectrum and for in situ probing of stress redistribution and relaxation processes. The quality and resolution of our results suggest that time-dependent material properties and key geometrical and kinematic source parameters of slow slip or deep creep episodes can be estimated in future source inversions based on spatiotemporal dv/v variations.

8. Conclusions

Our analysis of continuous seismic data from a regional network around the Anza seismic gap of the San Jacinto fault yields first-time observations of a complex pattern of episodic, tens-of-days-long seismic velocity variations dv/v along a continental strike-slip fault. The studied section of the San Jacinto fault exhibits a relatively shallow geodetic locking depth around 10 km (Jiang & Fialko, 2016; Lindsey et al., 2014), compared to the 14- to 18-km maximum depth of the background seismicity that occurs predominantly off the main faults (Ross et al., 2017; Trugman & Shearer, 2017). The potential of intermittent creep bursts in the transition zone below the locked fault (Wdowinski, 2009) is suggested by unusually elongated aftershock zones around moderate events (Meng & Peng, 2016; Ross et al., 2017). The spatial and temporal velocity variations observed in this work together with the long base strainmeter signals likely reflect strain transients that are associated with two deep creep episodes that are triggered by the remote M7.2 EMC earthquake and the local M5.4 Collins Valley earthquake (Inbal et al., 2017). Our data suggest an evolving medium response because the properties of the creep events inferred by Inbal et al. (2017) are more similar to each other than the amplitude and duration of the associated dv/v patterns imply. The results extend observations related to interaction mechanisms between different slip and deformation modes along faults that are typically obtained from satellite, geodetic, and seismicity data (Donnellan et al., 2014; Inbal et al., 2017; Jolivet et al., 2015; Khoshmanesh et al., 2015; Khoshmanesh & Shirzaei, 2018; Linde et al., 1996; Meng & Peng, 2016; Rousset et al., 2016). Seismic noise-based estimates of the associated velocity changes complement the array of observation techniques that can be used to study the coupling behavior along strike and down dip of the seismogenic zone and relaxation processes in the surrounding crust. Future joint inversions of GPS, satellite, seismic velocity change, and seismicity and tremor data for key parameters of deformation events can improve the constraints on evolving crustal and fault rheology and provide new insights on fault and earthquake interactions, triggering, stress redistribution, and feedback processes between stable and unstable slip modes.

Acknowledgments
We thank A. Inbal and J.-P. Ampuero for discussions and data sharing. We thank the reviewers B. Carpenter and J. Chaput, the Associate Editor N. Nakata, and the Editor M. Savage for comments that helped to improve the manuscript. G. Hillers acknowledges support through a Heisenberg Fellowship from the German Research Foundation (HI 1714/1-2). This project has received funding from the European Research Council (ERC) under the European Union's Horizon 2020 Research and Innovation Program (grant agreement 742335, F-IMAGE). Y. Ben-Zion acknowledges support from the Department of Energy (award DE-SC0016520). The facilities of the IRIS Data Management System, and specifically the IRIS Data Management Center, were used for access to waveform and metadata required in this study. Retrieval of the original seismograms from the IRIS DMS is sufficient to understand, evaluate, replicate, and build upon the reported research. The IRIS DMS is funded through the National Science Foundation and specifically the GEO Directorate through the Instrumentation and Facilities Program of the National Science Foundation under cooperative agreement EAR-1063471. The laser strainmeter data can be accessed at the IRIS Data Management Center (http://ds.iris.edu/pbo/processed/lsm/pinonflat4cs2008/). The MATLAB implementation of the Singular Value Decomposition based Wiener filter can be obtained from L. Moreau's website (https://isterre.fr/annuaire/pages-web-du-personnel/ludovic-moreau/article/codes-available-for-downloading).

References

Allam, A. A., & Ben-Zion, Y. (2012). Seismic velocity structures in the Southern California plate-boundary environment from double-difference tomography. *Geophysical Journal International*, *190*, 1181–1196. https://doi.org/10.1111/j.1365-246X.2012.05544.x

Anache-Ménier, D., van Tiggelen, B. A., & Margerin, L. (2009). Phase statistics of seismic coda waves. *Physical Review Letters*, *102*(24), 248–501. https://doi.org/10.1103/PhysRevLett.102.248501

Bensen, G. D., Ritzwoller, M. H., Barmin, M. P., Levshin, A. L., Lin, F., Moschetti, M. P., et al. (2007). Processing seismic ambient noise data to obtain reliable broad-band surface wave dispersion measurements. *Geophysical Journal International*, *169*, 1239–1260. https://doi.org/10.1111/j.1365-246X.2007.03374.x

Brenguier, F., Campillo, M., Takeda, T., Aoki, Y., Shapiro, N. M., Briand, X., et al. (2014). Mapping pressurized volcanic fluids from induced crustal seismic velocity drops. *Science*, *345*, 80–82. https://doi.org/10.1126/science.1254073

Brenguier, F., Shapiro, N. M., Campillo, M., Ferrazzini, V., Duputel, Z., Coutant, O., & Nercessian, A. (2008). Towards forecasting volcanic eruptions using seismic noise. *Nature Geoscience*, *1*, 126–130. https://doi.org/10.1038/ngeo104

Campillo, M. (2006). Phase and correlation of 'random' seismic fields and the reconstruction of the Green function. *Pure and Applied Geophysics*, *163*, 475–502. https://doi.org/10.1007/s00024-005-0032-8

Cheng, Y., Ross, Z. E., & Ben-Zion, Y. (2018). Diverse volumetric faulting patterns in the San Jacinto fault zone. *Journal of Geophysical Research: Solid Earth*, *123*, 5068–5081. https://doi.org/10.1029/2017JB015408

Clarke, D., Zaccarelli, L., Shapiro, N. M., & Brenguier, F. (2011). Assessment of resolution and accuracy of the Moving Window Cross Spectral technique for monitoring crustal temporal variations using ambient seismic noise. *Geophysical Journal International*, *186*, 867–882. https://doi.org/10.1111/j.1365-246X.2011.05074.x

Clements, T., & Denolle, M. A. (2018). Tracking groundwater levels using the ambient seismic field. *Geophysical Research Letters*, *45*, 6459–6465. https://doi.org/10.1029/2018GL077706

Colombi, A., Chaput, J., Brenguier, F., Hillers, G., Roux, P., & Campillo, M. (2014). On the temporal stability of the coda of ambient noise correlations. *Comptes Rendus Geoscience*, *346*, 307–316. https://doi.org/10.1016/j.crte.2014.10.002

Donnellan, A., Parker, J., Heflin, M., Lyzenga, G., Moore, A., Ludwig, L. G., et al. (2018). Fracture advancing step tectonics observed in the Yuha Desert and Ocotillo, CA, following the M_w7.2 El Mayor-Cucapah earthquake. *Earth and Space Science*, *5*, 456–472. https://doi.org/10.1029/2017EA000351

Donnellan, A., Parker, J., Hensley, S., Pierce, M., Wang, J., & Rundle, J. (2014). UAVSAR observations of triggered slip on the Imperial, Superstition Hills, and East Elmore Ranch Faults associated with the 2010 *M* 7.2 El Mayor Cucapah earthquake. *Geochemistry, Geophysics, Geosystems*, *15*, 815–829. https://doi.org/10.1002/2013GC005120

Duputel, Z., Ferrazzini, V., Brenguier, F., Shapiro, N., Campillo, M., & Nercessian, A. (2009). Real time monitoring of relative velocity changes using ambient seismic noise at the Piton de la Fournaise volcano (La Réunion) from January 2006 to June 2007. *Journal of Volcanology and Geothermal Research*, *184*, 164–173. https://doi.org/10.1016/j.jvolgeores.2008.11.024

Fang, H., Zhang, H., Yao, H., Allam, A., Zigone, D., Ben-Zion, Y., et al. (2016). A new algorithm for three-dimensional joint inversion of body wave and surface wave data and its application to the Southern California plate boundary region. *Journal of Geophysical Research: Solid Earth*, *121*, 3557–3569. https://doi.org/10.1002/2015JB012702

Gerstoft, P., & Tanimoto, T. (2007). A year of microseisms in Southern California. *Geophysical Research Letters*, *34*, L20304. https://doi.org/10.1029/2007GL031091

Gómez-García, C., Brenguier, F., Boué, P., Shapiro, N., Droznin, D., Droznina, S., et al. (2018). Retrieving robust noise-based seismic velocity changes from sparse data sets: Synthetic tests and application to Klyuchevskoy volcanic group (Kamchatka). *Geophysical Journal International*, *214*, 1218–1236. https://doi.org/10.1093/gji/ggy190

Grêt, A., Snieder, R., Aster, R. C., & Kyle, P. R. (2005). Monitoring rapid temporal change in a volcano with coda wave interferometry. *Geophysical Research Letters*, *32*, L06304. https://doi.org/10.1029/2004GL021143

Hadziioannou, C., Larose, E., Coutant, O., Roux, P., & Campillo, M. (2009). Stability of monitoring weak changes in multiply scattering media with ambient noise correlations: Laboratory experiments. *The Journal of the Acoustical Society of America*, *125*(6), 3688–3695. https://doi.org/10.1121/1.3125345

Hauksson, E., Stock, J., Hutton, K., Yang, W., Vidal-Villegas, J. A., & Kanamori, H. (2011). The 2010 M_w 7.2 El Mayor-Cucapah earthquake sequence, Baja California, Mexico and Southernmost California, USA: Active seismotectonics along the Mexican Pacific Margin. *Pure and Applied Geophysics*, *168*, 1255–1277. https://doi.org/10.1007/s00024-010-0209-7

Hauksson, E., Yang, W., & Shearer, P. M. (2012). Waveform relocated earthquake catalog for Southern California (1981 to June 2011). *Bulletin of the Seismological Society of America*, *102*(5), 2239–2244. https://doi.org/10.1785/0120120010

Hennino, R., Trégourès, N., Shapiro, N. M., Margerin, L., Campillo, M., van Tiggelen, B. A., & Weaver, R. L. (2001). Observation of equipartitioning of seismic waves. *Physical Review Letters*, *86*(15), 3447–3450. https://doi.org/10.1103/PhysRevLett.86.3447

Herrmann, R. B. (2013). Computer programs in seismology: An evolving tool for instruction and research. *Seismological Research Letters*, *84*(6), 1081–1088. https://doi.org/10.1785/0220110096

Hillers, G., & Ben-Zion, Y. (2011). Seasonal variations of observed noise amplitudes at 2–18 Hz in Southern California. *Geophysical Journal International*, *184*, 860–868. https://doi.org/10.1111/j.1365-246X.2010.04886.x

Hillers, G., Ben-Zion, Y., Campillo, M., & Zigone, D. (2015). Seasonal variations of seismic velocities in the San Jacinto fault area observed with ambient seismic noise. *Geophysical Journal International*, *202*, 920–932. https://doi.org/10.1093/gji/ggv151

Hillers, G., Ben-Zion, Y., Landès, M., & Campillo, M. (2013). Interaction of microseisms with crustal heterogeneity: A case study from the San Jacinto fault zone area. *Geochemistry, Geophysics, Geosystems*, *14*, 2182–2197. https://doi.org/10.1002/ggge.20140

Hillers, G., Campillo, M., Lin, Y.-Y., Ma, K.-F., & Roux, P. (2012). Anatomy of the high-frequency ambient seismic wave field at the TCDP borehole. *Journal of Geophysical Research*, *117*, B06301. https://doi.org/10.1029/2011JB008999

Hillers, G., Campillo, M., & Ma, K.-F. (2014). Seismic velocity variations at TCDP are controlled by MJO driven precipitation pattern and high fluid discharge properties. *Earth and Planetary Science Letters*, *391*, 121–127. https://doi.org/10.1016/j.epsl.2014.01.040

Hillers, G., Husen, S., Obermann, A., Planès, T., Larose, E., & Campillo, M. (2015). Noise-based monitoring and imaging of aseismic transient deformation induced by the 2006 Basel reservoir stimulation. *Geophysics*, *80*(4), 51–68. https://doi.org/10.1190/GEO2014-0455.1

Hillers, G., Retailleau, L., Campillo, M., Inbal, A., Ampuero, J.-P., & Nishimura, T. (2015). In situ observations of velocity changes in response to tidal deformation from analysis of the high-frequency ambient wavefield. *Journal of Geophysical Research: Solid Earth*, *120*, 210–225. https://doi.org/10.1002/2014JB011318

Hobiger, M., Wegler, U., Shiomi, K., & Nakahara, H. (2012). Coseismic and postseismic elastic wave variations caused by the 2008 Iwate-Miyagi Nairiku earthquake, Japan. *Journal of Geophysical Research*, *117*, B09313. https://doi.org/10.1029/2012JB009402

Hobiger, M., Wegler, U., Shiomi, K., & Nakahara, H. (2014). Single-station cross-correlation analysis of ambient seismic noise: Application to stations in the surroundings of the 2008 Iwate-Miyagi Nairiku earthquake. *Geophysical Journal International*, *198*, 90–109. https://doi.org/10.1093/gji/ggu115

Hudnut, K., Seeber, L., Rockwell, T., Goodmacher, J., Klinger, R., Lindvall, S., & McElwain, R. (1989). Surface ruptures on cross-faults in the 24 November 1987 Superstition Hills, California, earthquake sequence. *Bulletin of the Seismological Society of America*, *79*(2), 282–296.

Inbal, A., Ampuero, J.-P., & Avouac, J.-P. (2017). Locally and remotely triggered aseismic slip on the central San Jacinto Fault near Anza, CA, from joint inversion of seismicity and strainmeter data. *Journal of Geophysical Research: Solid Earth*, *122*, 3033–3061. https://doi.org/10.1002/2016JB013499

Inbal, A., Cristea-Platon, T., Ampuero, J.-P., Hillers, G., Agnew, D., & Hough, S. E. (2018). Sources of long-range anthropogenic noise in Southern California and implications for tectonic tremor detection. *Bulletin of the Seismological Society of America*, *108*(6), 3511–3527. https://doi.org/10.1785/0120180130

Jiang, J., & Fialko, Y. (2016). Reconciling seismicity and geodetic locking depths on the Anza section of the San Jacinto fault. *Geophysical Research Letters*, *43*, 10,663–10,671. https://doi.org/10.1002/2016GL071113

Johnson, P. A., & Jia, X. (2005). Nonlinear dynamics, granular media and dynamic earthquake triggering. *Nature*, *437*(6), 871–874. https://doi.org/10.1038/nature04015

Jolivet, R., Candela, T., Lasserre, C., Renard, F., Klinger, Y., & Doin, M.-P. (2015). The burst-like behavior of aseismic slip on a rough fault: The creeping section of the Haiyuan fault, China. *Bulletin of the Seismological Society of America*, *105*(1), 480–488. https://doi.org/10.1785/0120140237

Khoshmanesh, M., & Shirzaei, M. (2018). Episodic creep events on the San Andreas Fault caused by pore pressure variations. *Nature Geoscience*, *11*, 610–614. https://doi.org/10.1038/s41561-018-0160-2

Khoshmanesh, M., Shirzaei, M., & Nadeau, R. M. (2015). Time-dependent model of aseismic slip on the central San Andreas Fault from InSAR time series and repeating earthquakes. *Journal of Geophysical Research: Solid Earth*, *120*, 6658–6679. https://doi.org/10.1002/2015JB012039

Larose, E., Roux, P., & Campillo, M. (2007). Reconstruction of Rayleigh-Lamb dispersion spectrum based on noise obtained from an air-jet forcing. *The Journal of the Acoustical Society of America*, *122*(6), 3437–3444. https://doi.org/10.1121/1.2799913

Lewis, M. A., Peng, Z., Ben-Zion, Y., & Vernon, F. L. (2005). Shallow seismic trapping structure in the San Jacinto fault zone near Anza, California. *Geophysical Journal International*, *162*, 867–881. https://doi.org/10.1111/j.1365-246X.2005.02684.x

Li, Y.-G., & Vernon, F. L. (2001). Characterization of the San Jacinto fault zone near Anza, California, by fault zone trapped waves. *Journal of Geophysical Research*, *106*(B12), 30,671–30,688. https://doi.org/10.1029/2000JB000107

Linde, A. T., Gladwin, M. T., Johnston, M. J. S., Gwyther, R. L., & Bilham, R. G. (1996). A slow earthquake sequence on the San Andreas fault. *Nature*, *383*, 65–68.

Lindsey, E. O., Sahakian, V. J., Fialko, Y., Bock, Y., Barbot, S., & Rockwell, T. K. (2014). Interseismic strain localization in the San Jacinto fault zone. *Pure and Applied Geophysics*, *171*, 2937–2954. https://doi.org/10.1007/s00024-013-0753-z

Lobkis, O. I., & Weaver, R. L. (2003). Coda-wave interferometry in finite solids: Recovery of *P*-to-*S* conversion rates in an elastodynamic billiard. *Physical Review Letters*, *90*(25), 254302. https://doi.org/10.1103/PhysRevLett.90.254302

Lyakhovsky, V., Hamiel, Y., Ampuero, J.-P., & Ben-Zion, Y. (2009). Nonlinear damage rheology and wave resonance in rocks. *Geophysical Journal International*, *178*, 910–920. https://doi.org/10.1111/j.1365-246X.2009.04205.x

Mai, P., & Thingbaijam, K. (2014). SRCMOD: An online database of finite-fault rupture models. *Seismological Research Letters*, *85*(6), 1348–1357. https://doi.org/10.1785/0220140077

Meng, X, & Peng, Z. (2014). Seismicity rate changes in the Salton Sea Geothermal Field and the San Jacinto fault zone after the 2010 M_w 7.2 El Mayor-Cucapah earthquake. *Geophysical Journal International*, *197*, 1750–1762. https://doi.org/10.1093/gji/ggu085

Meng, X., & Peng, Z. (2016). Increasing lengths of aftershock zones with depths of moderate-size earthquakes on the San Jacinto fault suggests triggering of deep creep in the middle crust. *Geophysical Journal International*, *204*, 250–261. https://doi.org/10.1093/gji/ggv445

Moreau, L., Stehly, L., Boué, P., Lu, Y., & Campillo, M. (2017). Improving ambient noise correlation functions with an SVD-based Wiener filter. *Geophysical Journal International*, *211*, 418–426. https://doi.org/10.1093/gji/ggx306

Obermann, A., Froment, B., Campillo, M., Larose, E., Planès, T., Valette, B., et al. (2014). Seismic noise correlations to image structural and mechanical changes associated with the M_W 7.9 2008 Wenchuan earthquake. *Journal of Geophysical Research: Solid Earth*, *119*, 3155–3168. https://doi.org/10.1002/2013JB010932

Obermann, A., Planès, T., Hadziioannou, C., & Campillo M. (2016). Lapse-time-dependent coda-wave depth sensitivity to local velocity perturbations in 3-D heterogeneous elastic media. *Geophysical Journal International*, *207*, 59–66. https://doi.org/10.1093/gji/ggw264

Obermann, A., Planès, T., Larose, E., & Campillo, M. (2013). Imaging preeruptive and coeruptive structural and mechanical changes of a volcano with ambient seismic noise. *Journal of Geophysical Research: Solid Earth*, *118*, 6285–6294. https://doi.org/10.1002/2013JB010399

Obermann, A., Planès, T., Larose, E., & Campillo, M. (2019). 4-D imaging of subsurface changes with coda waves: Numerical studies of 3-D combined sensitivity kernels and application to the M_W7.9, 2008 Wenchuan earthquake. *Pure and Applied Geophysics*, *176*, 1243–1254. https://doi.org/10.1007/s00024-018-2014-7

Pacheco, C., & Snieder, R. (2005). Time-lapse travel time change of multiply scattered acoustic waves. *The Journal of the Acoustical Society of America*, *118*(3), 1300–1310. https://doi.org/10.1121/1.2000827

Paul, A., Campillo, M., Margerin, L., Larose, E., & Derode, A. (2005). Empirical synthesis of time-asymmetrical Green function from the correlation of coda waves. *Journal of Geophysical Research*, *110*, B08302. https://doi.org/10.1029/2004JB003521

Poli, P., Pedersen, H. A., Campillo, M., & POLENET/LAPNET Working Group (2012). Emergence of body waves from cross-correlation of short period seismic noise. *Geophysical Journal International*, *188*, 549–558. https://doi.org/10.1111/j.1365-246X.2011.05271.x

Poupinet, G., Ellsworth, W., & Frechet, J. (1984). Monitoring velocity variations in the crust using earthquake doublets: An application to the Calaveras Fault, California. *Journal of Geophysical Research*, *89*(B7), 5719–5731.

Richter, T., Sens-Schönfelder, C., Kind, R., & Asch, G. (2014). Comprehensive observation and modeling of earthquake and temperature-related seismic velocity changes in northern Chile with passive image interferometry. *Journal of Geophysical Research: Solid Earth*, *119*, 4747–4765. https://doi.org/10.1002/2013JB010695

Rivet, D., Campillo, M., Shapiro, N. M., Cruz-Atienza, V., Radiguet, M., Cotte, N., & Kostoglodov, V. (2011). Seismic evidence of nonlinear crustal deformation during a large slow slip event in Mexico. *Geophysical Research Letters*, *38*, L08308. https://doi.org/10.1029/2011GL047151

Ross, Z. E., Rollins, C., Cochran, E. S., Hauksson, E., Avouac, J.-P., & Ben-Zion, Y. (2017). Aftershocks driven by afterslip and fluid pressure sweeping through a fault-fracture mesh. *Geophysical Research Letters*, *44*, 8260–8267. https://doi.org/10.1002/2017GL074634

Rousset, B., Jolivet, R., Simons, M., Lasserre, C., Riel, B., Milillo, P., et al. (2016). An aseismic slip transient on the North Anatolian Fault. *Geophysical Research Letters*, *43*, 3254–3262. https://doi.org/10.1002/2016GL068250

Rymer, M. J., Boatwright, J., Seekins, L. C., Yule, J. D., & Liu, J. (2002). Triggered surface slips in the Salton Trough Associated with the 1999 Hector Mine, California, earthquake. *Bulletin of the Seismological Society of America*, *92*(4), 1300–1317.

Sanders, C. O., & Kanamori, H. (1984). A seismotectonic analysis of the Anza Seismic Gap, San Jacinto fault zone, Southern California. *Journal of Geophysical Research*, *89*(B7), 5873–5890.

Sens-Schönfelder, C., & Wegler, U. (2006). Passive image interferometry and seasonal variations of seismic velocities at Merapi Volcano, Indonesia. *Geophysical Research Letters*, *33*, L21302. https://doi.org/10.1029/2006GL027797

Sens-Schönfelder, C., & Wegler, U. (2011). Passive image interferometry for monitoring crustal changes with ambient seismic noise. *Comptes Rendus Geoscience*, *343*, 639–651. https://doi.org/10.1016/j.crte.2011.02.005

Shapiro, N. M., Campillo, M., Margerin, L., Singh, S. K., Kostoglodov, V., & Pacheco, J. (2000). The energy partitioning and the diffuse character of the seismic coda. *Bulletin of the Seismological Society of America*, *90*(3), 655–665.

Sharp, R. V. (1967). San Jacinto fault zone in the peninsular ranges of Southern California. *Geological Society of America Bulletin*, *78*, 705–730.

Stehly, L., Cupillard, P., & Romanowicz, B. (2011). Towards improving ambient noise tomography using simultaneously curvelet denoising filters and SEM simulations of seismic ambient noise. *Comptes Rendus Geoscience*, *343*, 591–599. https://doi.org/10.1016/j.crte.2011.03.005

Taira, T., Nayak, A., Brenguier, F., & Manga, M. (2018). Monitoring reservoir response to earthquakes and fluid extraction, Salton Sea geothermal field, California. *Science Advances*, *4*(1), 254302. https://doi.org/10.1126/sciadv.1701536

Tarantola, A., & Valette, B. (1982). Generalized nonlinear inverse problems solved using the least squares criterion. *Reviews of Geophysics*, *20*(2), 219–232.

Trugman, D. T., & Shearer, P. M. (2017). Application of an improved spectral decomposition method to examine earthquake source scaling in Southern California. *Journal of Geophysical Research: Solid Earth*, *122*, 2890–2910. https://doi.org/10.1002/2017JB013971

Tsai, V. C. (2011). A model for seasonal changes in GPS positions and seismic wave speeds due to thermoelastic and hydrologic variations. *Journal of Geophysical Research*, *116*, B04404. https://doi.org/10.1029/2010JB008156

Wang, Q.-Y., Brenguier, F., Campillo, M., Lecointre, A., Takeda, T., & Aoki, Y. (2017). Seasonal crustal seismic velocity changes throughout Japan. *Journal of Geophysical Research: Solid Earth*, *122*, 7987–8002. https://doi.org/10.1002/2017JB014307

Wdowinski, S. (2009). Deep creep as a cause for the excess seismicity along the San Jacinto fault. *Nature Geoscience*, *2*, 882–885. https://doi.org/10.1038/ngeo684

Weaver, R. L. (1982). On diffuse waves in solid media. *The Journal of the Acoustical Society of America*, *71*(6), 1608–1609.

Wei, S., Fielding, E., Leprince, S., Sladen, A., Avouac, J.-P., Helmberger, D., et al. (2011). Superficial simplicity of the 2010 El Mayor-Cucapah earthquake of Baja California in Mexico. *Nature Geoscience*, *4*, 615–618. https://doi.org/10.1038/ngeo1213

Wei, M., Sandwell, D., Fialko, Y., & Bilham, R. (2011). Slip on faults in the Imperial Valley triggered by the 4 April 2010 M_w 7.2 El Mayor-Cucapah earthquake revealed by InSAR. *Geophys Research Letters*, *38*, L01308. https://doi.org/10.1029/2010GL045235

Wessel, P., Smith, W. H. F., Scharroo, R., Luis, J., & Wobbe, F. (2013). Generic Mapping Tools: Improved version released. *EOS Trans AGU*, *94*, 409–410. https://doi.org/10.1002/2013EO450001

Zhan, Z., Tsai, V. C., & Clayton, R. W. (2013). Spurious velocity changes caused by temporal variations in ambient noise frequency content. *Geophysical Journal International*, *194*, 1574–1581. https://doi.org/10.1093/gji/ggt170

Zigone, D., Ben-Zion, Y., Campillo, M., & Roux, P. (2015). Seismic tomography of the Southern California plate boundary region from noise-based Rayleigh and Love waves. *Pure and Applied Geophysics*, *172*, 1007–1032. https://doi.org/10.1007/s00024-014-0872-1